USGS
science for a changing world

Characterizing Meteor Crater Impact Melts Through Geochemistry and Textural Analysis

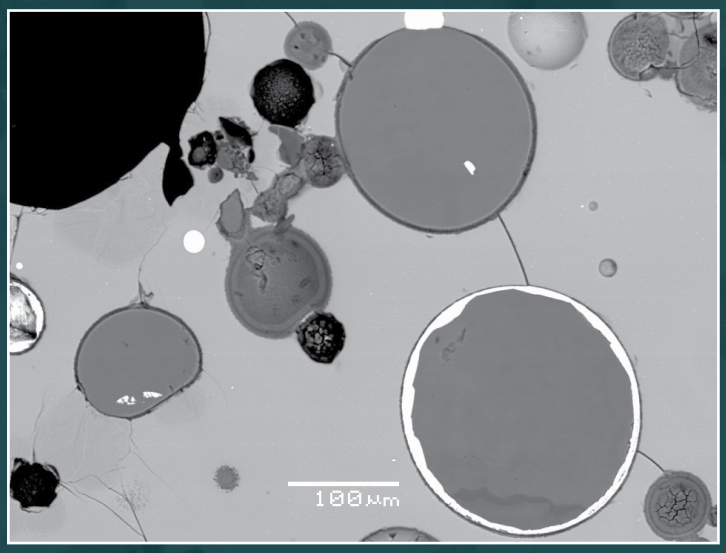

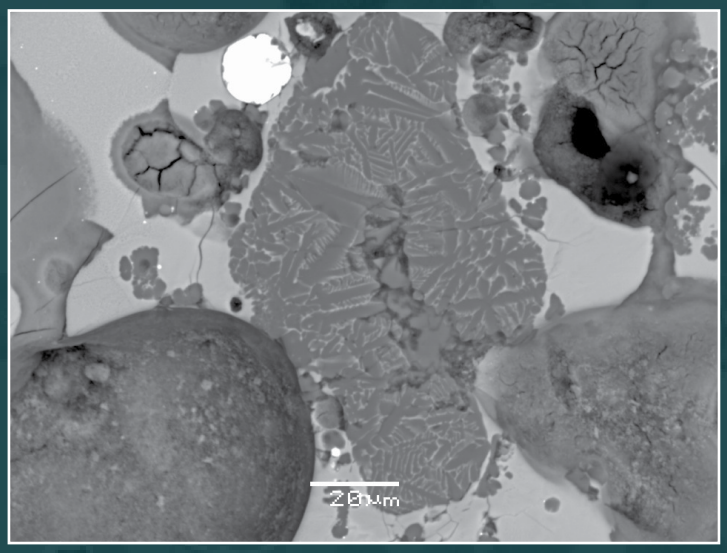

Open-File Report 2024–1062

U.S. Department of the Interior
U.S. Geological Survey

Cover: Scanning electron microscope images of impact melt fragments from Meteor Crater. The image on the left shows three carbonate inclusions; the leftmost and topmost carbonate inclusions have small inclusions of barium sulfate (visible as bright phases within the carbonate) and the third and largest carbonate inclusion has a barium sulfate rim. The image on the right shows a recrystallized silica grain that has skeletal dendritic habits and is surrounded by vesicles. Scale bars are in microns (μm).

Characterizing Meteor Crater Impact Melts Through Geochemistry and Textural Analysis

By Amber L. Gullikson, Tenielle A. Gaither, and Justin J. Hagerty

Open-File Report 2024–1062

U.S. Department of the Interior
U.S. Geological Survey

U.S. Geological Survey, Reston, Virginia: 2024

Suggested citation:
Gullikson, A.L., Gaither, T.A., and Hagerty, J.J., 2024, Characterizing Meteor Crater impact melts through geochemistry and textural analysis: U.S. Geological Survey Open-File Report 2024–1062, 23 p., https://doi.org/10.3133/ofr20241062.

Associated data for this publication:
Gullikson, A.L., Gaither, T.A., and Hagerty, J.J., 2024, Geochemistry and high-resolution backscattered electron imaging of Meteor Crater impact melts: U.S. Geological Survey data release, https://doi.org/10.5066/P9OGAJ8P.

ISSN 2331-1258 (online)

Acknowledgments

Funding for data collection and analysis were supported by NASA through the Planetary Geology and Geophysics program via grant NNH09AK43I. The publication of this Open-File Report and associated data release were funded through an inter-agency agreement between NASA and the U.S. Geological Survey Astrogeology Science Center. We would like to thank Lori Pigue, Greg Vaughan, and Jim Skinner for their helpful comments that have improved the clarity of this report.

Contents

Figures

Tables

Conversion Factors

International System of Units to U.S. customary units

Multiply	By	To obtain
	Length	
millimeter (mm)	0.03937	inch (in.)
meter (m)	3.281	foot (ft)
kilometer (km)	0.6214	mile (mi)

Abbreviations

BSE	backscattered electron
CIs	carbonate inclusions
EDS	energy dispersive X-ray spectrometry
MIs	metallic inclusions
SEM	scanning electron microscope
USGS	U.S. Geological Survey
WDS	wavelength dispersive spectrometry

Characterizing Meteor Crater Impact Melts Through Geochemistry and Textural Analysis

By Amber L. Gullikson, Tenielle A. Gaither, and Justin J. Hagerty

Abstract

The U.S. Geological Survey Astrogeology Science Center houses the Meteor Crater sample collection, an assemblage of over 2,500 meters of cuttings from 161 drill holes into Meteor Crater's rim, flanks, and ejecta blanket. We have utilized this unique collection to study the composition and spatial distribution of impact-generated materials from within the ejecta blanket. Meteor Crater has historically been known to have generated only a relatively small amount of impact melt compared to other terrestrial craters of similar size. A detailed compositional and textural dataset of impact-derived melts from this impact can therefore be a useful asset in improving our understanding of crater formation, and in particular impact melt formation.

We have characterized 42 impact-melt particles from Meteor Crater using a scanning electron microscope and an electron microprobe for textural and compositional analysis. We analyzed samples from six drill holes in the ejecta blanket, situated to the northwest, southeast, south, and southwest of the crater (ejecta northeast of the crater is devoid of impact melts). Impact melts were collected from drill cuttings at various depths within the ejecta blanket, ranging from a few centimeters below the surface down to ~6.5 meters.

Backscattered electron (BSE) images were acquired for each analyzed impact-melt particle. To characterize the various textures and phases present in each impact melt, we also took many detailed BSE images. Our geochemical analyses include full spectral profiles using energy dispersive X-ray spectrometry and well-calibrated wavelength dispersive spectrometry for a number of phases, including minerals (olivine, pyroxene, and so on), pristine glass, and metallic inclusions. The full dataset is available in ScienceBase as a data release (Gullikson and others, 2024), accessible at https://doi.org/10.5066/P9OGAJ8P.

Our goal for this Open-File Report is to provide a summary of this immense dataset, details on data collection, descriptions of the different phases observed within impact-melt particles (both geochemically and texturally), and observable trends.

Introduction

Impact cratering is a fundamental process that affects planetary bodies throughout the solar system. One aspect of impact cratering that heavily influences the provenance of materials on planetary surfaces is the creation and distribution of impact ejecta (Hermalyn and others, 2008). Studies of impact ejecta are essential for providing a framework for understanding and reconstructing the formation and histories of impact craters (Grant and Schultz, 1990). The results of such studies can often be extended to the characterization of craters on other planetary bodies. Knowledge of the distribution of ejecta (a function of impactor size, velocity, and trajectory, as well as the composition and coherence of the target lithologies) can be used to place constraints on impact cratering models (Roddy and others, 1975; Melosh, 1980, 1989), which in turn can help to develop an understanding of how planetary surfaces are affected by impact cratering. Efforts to understand the complexity of impact ejecta deposits and the structure of impact craters on other planetary bodies have led to an increased emphasis on analysis of terrestrial impact craters as analogs for impact cratering processes.

Impact melts are mixtures of melted target rock and the projectile, and they are an important component of impact ejecta deposits. They form when the shock wave generated by an impact travels through and transmits energy into the target rock. Once the shock wave has passed and the pressure exponentially drops, the target rock almost instantaneously melts, along the with the projectile (Melosh, 1989). The melted target rock and projectile are transported with the overall movement of the fractured target rock, driven downward and outward toward the transient crater floor. After the melt reaches the transient floor, it moves upward and outward along the floor (Grieve and others, 1977), and as it moves, it mixes with variably shocked lithic material. This process of mixing impact-generated target rock and projectile melts with variable amounts of lithic material can produce ballistically ejected small glassy bodies, metallic spherules, impact-melt breccias, and sheets, dikes, and sills of impact melt in the near-crater environment (see, for example, Shoemaker, 1960; Kelly and others, 1974; Hörz and others, 2002; Mittlefehldt and others, 2005; Kring, 2007; Newsom and others, 2012).

Geologic Setting of Meteor Crater

Impact Event and Physical Parameters

Meteor Crater is a bowl-shaped depression 180 meters (m) deep and 1.2 kilometers (km) in diameter located on the southern edge of the Colorado Plateau in north-central Arizona (Shoemaker and Kieffer, 1974). This impact crater formed ~50,000 years ago (Nishiizumi and others, 1991; Phillips and others, 1991) by the impact of a 100,000-ton iron-nickel meteorite, ~30 m in diameter, which struck at a speed estimated to be between 12 and 20 km per second (Shoemaker, 1960; Melosh, 1980; 1989; Melosh and Collins, 2005; Artemieva and Pierazzo, 2009). The crater and surrounding rim have since experienced limited erosion, making Meteor Crater one of the best preserved, young impact craters on Earth (Roddy and others, 1975; Grant and Schultz, 1993, Ramsey, 2002). Structural controls in the target rocks, induced by scissor-faulting of mutually perpendicular joints oriented northwest-southeast and northeast-southwest, give Meteor Crater a pseudo-rectangular shape in map view (fig. 1) (Shoemaker, 1960; Roddy, 1978; Ramsey, 1995).

Target Lithologies

Near Meteor Crater, the surface of the Colorado Plateau has very low relief and is underlain by ~1,200 m of nearly flat-lying beds of Paleozoic and Mesozoic strata that overlie pre-Cambrian crystalline basement (Shoemaker and Kieffer, 1974; Roddy and others, 1975). Target rocks from top to bottom include a thin veneer of partly eroded Triassic Moenkopi Formation (0–23 m thick), Permian Kaibab Formation (80–95 m thick), Permian Toroweap Formation (2–3 m thick), and Permian Coconino Sandstone (220 m thick), underlain by the Pennsylvanian and Permian Supai Group rocks (300 m thick; Shoemaker, 1960; Shoemaker and Kieffer, 1974). Detailed descriptions of the target rocks are presented by Shoemaker (1960), Shoemaker and Kieffer (1974), Roddy and others (1975), and Kring (2007).

Meteor Crater Impact Melts

Meteor Crater has historically been described as having a small amount of impact melt compared to other craters of similar size (Nininger, 1956; Shoemaker, 1960; Melosh, 1989). The apparent relative lack of impact melt has been attributed to everything from the volatile content of the target rock to the velocity of the impactor (Hörz and others, 2002; Melosh and Collins, 2005). Impact melt types at Meteor Crater include (1) ballistically dispersed melt bombs (~centimeter-sized) comprising mixtures of melted target rock and melted projectile; (2) shock-melted Coconino Sandstone rocks (for example, lechatelierite) found in the crater floor beneath alluvium and in the ejecta blanket; and (3) ballistically dispersed metallic spherules (for example, melt droplets from the Canyon Diablo meteorite, the impactor that created Meteor Crater). Though all these different melt types have been studied for decades, investigations by Hörz and others (2002), See and others (2002), and Mittlefehldt and others (2005) provided the first detailed chemical information about ballistically dispersed impact-melt particles at Meteor Crater.

See and others (2002) focused on major elemental analyses of the target rocks at Meteor Crater, and Hörz and others (2002) and Mittlefehldt and others (2005) carried out geochemical analyses of impact-melt particles and metallic spherules. Target rocks used in these studies were sampled either from within the crater or the overturned flap; impact-melt particles and metallic spherules were obtained from the Nininger Collection, archived at the Arizona State University Center for Meteorite Studies (Hörz and others, 2002; See and others, 2002; Mittlefehldt and others, 2005). The ballistically ejected materials were originally collected from the plains surrounding the crater, though no precise coordinates were recorded.

Impact-melt particles from this collection were commonly oxidized and (or) hydrated, likely occurring over the tens of thousands of years being exposed on (or close to) the surface. Pristine glass within these particles is rare. Hörz and others (2002) recovered few fragments that contained pristine glass; they described them as texturally homogeneous, clear in color, but compositionally heterogeneous, both within individual particles and from sample to sample. Based on geochemistry, Hörz and others (2002) divided the impact-melt particles into three compositional groups, inferring that these groups likely represented different target rock proportions (as well as meteoritic component) and therefore different depths of melting. Hörz and others (2002) suggested that either all three compositionally distinct melts were derived from a depth of <30 m, or that one group (a mixture of Moenkopi and Kaibab Formation rocks and a small amount of meteorite) was sourced at shallow depth and the other two (higher content of meteorite and Kaibab Formation rocks, with the addition of Coconino Sandstone rocks) originated from depths >90 m.

Additional geochemical analyses on impact-melt particles, including trace elements, were carried out by Mittlefehldt and others (2005). Their results indicated a melt zone that contained variable amounts of Moenkopi Formation, Kaibab Formation, and meteorite, with little to no input from Coconino Sandstone or Toroweap Formation rocks. It is important to note that analytical techniques differed between the Mittlefehldt and Hörz studies: Mittlefehldt and others (2005) measured bulk chemical analyses of the impact-melt particles, whereas Hörz and others (2002) used X-ray elemental maps and quantitative individual mineral and glass measurements. Different techniques may result in discrepancies between estimated depth of melting or input of differing target rock proportions.

The addition of impact melt analyses with known locations—both lateral distances from the crater and vertical depths within the ejecta blanket (compared to the previously studied impact melts that were collected on the surface without their locations recorded)—can be used to test how robust the melting depth hypotheses of Hörz and others (2002) and Mittlefehldt and others (2005) are and provide further information on the characteristics of impact-melt deposits at Meteor Crater. Furthermore, impact-melt particles sampled at depth from within the ejecta blanket can help determine whether impact cratering conditions allowed

carbonate-rich rocks to undergo melting (retaining some CO_2), as opposed to exclusive devolatilization (all CO_2 vaporized), as well as the prevalence of secondary alteration at depth.

Meteor Crater Sample Collection

The U.S. Geological Survey (USGS) Astrogeology Science Center curates and houses the Meteor Crater sample collection. This collection includes more than 2,500 m of cuttings from 161 holes that were drilled into the crater's rim, flanks, and ejecta blanket (Roddy and others, 1975). Depth of drill holes ranges from a few meters down to ~50 m, sampling material every ~0.3 m. A digital database detailing pertinent information for each collected sample (from the 161 drill holes), including drill hole identification number, depth, amount collected, and so on, has been made available through ScienceBase (a USGS trusted long-term data repository) as a published data release (Gaither and others, 2023).

Meteor Crater is an excellent terrestrial analog for studying planetary impact cratering dynamics, such as complex impact crater formation and morphology, impact-induced hydrothermal systems, impact melting of sedimentary target rocks, and mineral shock metamorphism. The USGS Meteor Crater sample collection provides the planetary science community free access to these geologic samples for petrographic, geochemical, structural, and other geologic analyses. Given the modern financial and logistical difficulties inherent in conducting thorough sampling campaigns at impact sites, continued preservation of this geologic collection and increasing access to the samples by the scientific community maximizes the prior financial and scientific investments of the USGS and NASA.

Work presented here utilized the Meteor Crater sample collection to characterize composition and textural information of impact-melt particles generated during the meteorite impact. Through this publication we showcase some of the unique impact-melt particles that were analyzed, including some uncommon features, such as lechatelierite (shock-melted Coconino Sandstone), to promote future research and use of this unique collection. Information on requesting samples from this collection can be found in Gaither and others (2023), as well as at https://www.usgs.gov/centers/astrogeology-science-center/science/meteor-crater-sample-collection.

Purpose and Scope

The purpose of this study was to characterize impact-melt particles generated during the formation of Meteor Crater and emplaced within the ejecta blanket. Utilizing the Meteor Crater sample collection granted us the ability to study composition and spatial distribution (both laterally and vertically) of impact-melt particles with known locations. Such information can lead to better understanding the role of volatiles, depth of melting, and chemical fractionation when impacts occur in sedimentary environments. Additionally, selection of samples from deep within the ejecta blanket increased our chances of analyzing particles that have experienced less alteration since emplacement, compared to impact melts collected on or near the surface. The scope of this publication is to summarize the findings of our geochemical and textural analyses. Forty-two impact-melt particles were analyzed, and presented here are common textures we observed among phases (both glass and minerals), averaged compositions, and geochemical trends. The full dataset of all backscattered electron (BSE) images and geochemical data is available as a data release (Gullikson and others, 2024) and can be found at https://doi.org/10.5066/P9OGAJ8P.

Methods

Sample Selection and Preparation

The Meteor Crater sample collection has rock cuttings from 161 drilling locations; we narrowed down our sample selection to those from six drill holes: numbers 42, 45, 60, 94, 95, and 109 (fig. 1). These drill holes were noted to have a higher concentration of impact melt compared to other drill holes examined by Gullikson and others (2016). As part of our initial work described in Gullikson and others (2016), we sieved drill cuttings from these selected drill holes into different sizes, and any particles 5 millimeters (mm) in diameter and greater were separated into their respective lithologies (including impact-melt particles). A subset of these impact-melt particles, which typically ranged 5–10 mm in diameter, were then collected for further analysis. These particles all had a glassy appearance but varied in color (black, red, and yellow/orange). Most particles were collected from depths ranging from ~0.5 to 6 m below the surface. To conserve samples for future research, we limited our selection to 42 impact-melt particles for analysis. The samples chosen were considered to appropriately represent the impact melt population within the Meteor Crater ejecta blanket based on a qualitative assessment of size, shape, and color of the impact-melt particles first identified in the Gullikson and others (2016) work. It should be noted that there were many small (<5 mm), dark colored particles within the ejecta deposits that resembled impact-melt beads (spherical in shape), but upon further analysis they were identified as iron concretions. Due to time limitations, it was beyond the scope of this work to separate small impact-melt particles from these post-impact iron concretions; therefore, we focused on particles of sufficient size (that is, ≥5 mm) whose identification was easier to resolve.

Drill hole number and sample depth were recorded for each particle to preserve their original geolocation. Particles were gently broken into several pieces to expose their interiors, then placed into small cylindrical sample cups, and epoxy was poured into each cup. Cups were then placed in a vacuum to remove any bubbles. After epoxy cured and hardened, samples were extracted from sample cups and polished down until most of the individual fragments were exposed at the surface. We then used increasingly finer-sized grit sandpaper to polish until the sample had a smooth and even surface without any noticeable scratches. Between the change of grit size and after the final polish, samples were placed in an ultrasonic portable

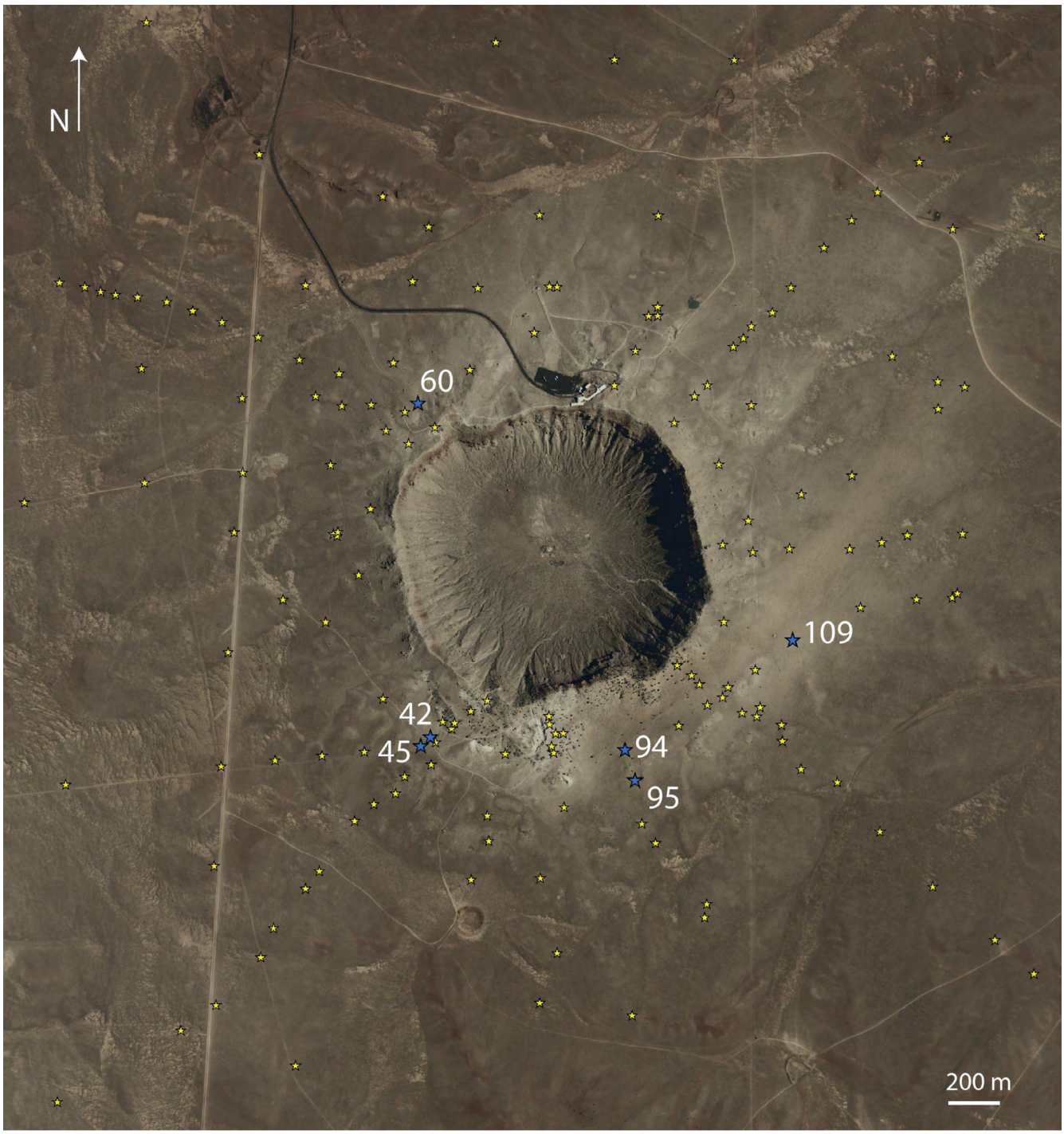

Figure 1. Satellite image of Meteor Crater. Star symbols (yellow and blue) represent all drilling locations (Roddy and others, 1975). Blue stars show locations of drill holes used in this study and their respective drill hole numbers. Image credit: NAD83/UTM zone 12N map, National Agriculture Imagery Program, 2007.

cleaner with deionized water to remove any foreign substances (that is, remnants from the polishing process). Each mount comprises a single impact-melt particle, broken into several smaller fragments, with interior surfaces exposed and polished for geochemical and imaging analyses (fig. 2). Sample names were assigned a letter in the order they were collected, such that the first sample identifier is mount A, the second is mount B, and so forth.

Geochemistry and Imaging

We used a scanning electron microscope (SEM) at Northern Arizona University for BSE imaging and energy dispersive X-ray spectrometry (EDS) to characterize our samples both texturally and compositionally. Standards used for calibration are listed in Gullikson and others (2024). “Quick” qualitative analyses, where a spectrum of characteristic X-ray patterns is

obtained, were regularly done alongside BSE imaging to identify the phases present (referring to both mineral phases and pristine versus altered glass). For more accurate measurements, we ran full spectral profiles at longer count rates to detail a phase's composition (specifically elemental percentages).

Using our EDS and BSE data, we identified the most representative samples for pristine glass, banded glass (alteration/hydration texture), metallic inclusions, barium sulfate, and carbonate inclusions for more precise measurements. Using an electron microprobe at Northern Arizona University, we carried out these analyses with wavelength dispersive spectrometry (WDS). WDS allows an increase in count rates, a lower detection limit for light elements (increasing resolution and precision for such elements), and a lower energy resolution that is ideal for providing reproduceable and reliable results for the selected phases.

Prior to analysis, samples were carbon coated to prevent charging (the accumulation of a negative charge on the sample from the incident beam) while in the instrument. For each phase analyzed, a specific set of standards was used for calibration. Calibration was tested periodically during data collection to ensure that the instrument's precision did not diminish over time. Instrument settings were changed depending on which phase was being analyzed. For example, glass analysis settings were 20.1 nanoampere (nA) beam current and 14.8 volts; settings for the analysis of carbonate inclusions were 10 nA beam current and 15 volts; and metallic inclusions were 50 nA beam current and 20 volts.

Ideally, oxide concentrations for spot analyses should equal 100 percent. There are a number of reasons why these analyses might yield higher or lower percentages, such as an unfocused incident electron beam when taking measurements, beam positioning (overlapping two phases), alteration (hydration), or that another element is present that was not included in the calibration. Therefore, analyses that resulted in totals of 97 percent or less, or 102 percent or more, were considered unreliable and not used. We anticipated our banded glass samples to return low totals because of alteration, though we still carried out these measurements for comparison to pristine glass.

Results

As shown in figure 2, each mount is composed of fragments from only one impact-melt particle. BSE images were acquired for all 42 mounts, including overview images for each fragment within a mount and high-resolution images that captured and detailed the textures and minerals observed. Full spectral profiles using EDS were collected for olivine, pyroxene, carbonate inclusions, glass, and "other phases," which refers to unique or uncommon features (phases observed in only one or a few particles). Compositional analyses using WDS were done for glass, carbonate inclusions, metallic inclusions, and barium sulfate.

All BSE images and geochemical data—including all compositional data, sorted first by technique (EDS and WDS), then by analyzed phase—have been published and made available in ScienceBase (Gullikson and others, 2024). All the data are available as .csv files. BSE images for each mount have been grouped into individual .pdf files; the first two pages in each file include a binocular microscope image of the full mount, with each fragment numbered, and a summary page that lists what phases were identified in each fragment using the SEM. Individual images used in the .pdf files can also be found as. jpegs under "child items" in this data release.

Figure 2. Photographs showing impact-melt particles in epoxy mounts used in this study. In the upper left of images is the sample identifier, drill hole number, and depth (in meters).

The following results showcase the rich amount of material made available in the Gullikson and others (2024) data release. We summarize here the textures and geochemistry of the major phases present in our set of Meteor Crater impact-melt particles and encourage users to explore this dataset in more detail.

Pristine Glass

Texture

Nearly 75 percent of samples had measurable amounts of pristine glass. Pristine glass typically had submicron metallic inclusions (Fe-Ni in composition) dispersed throughout the samples, though finding large spot sizes free of inclusions for geochemical analyses was not difficult (fig. 3*A–C*). Of the nearly 75 percent of samples with pristine glass, 30 percent had olivine crystals within the glass that ranged from acicular to skeletal in shape (fig. 3*C–D*).

Compositional Data

We analyzed 15 impact-melt particles that had pristine glass. These samples were collected from drill holes 45, 60, 94, and 95 (fig. 1) and ranged in depth from ~0.5 to 6.4 m. Following a similar approach to Hörz and others (2002, their fig. 10), we averaged glass compositions for each particle (table 1) and plotted them on a ternary diagram (fig. 4) to get a better sense of how much target rock and meteorite contributed to the melts. The apices are FeO+NiO (representing the meteorite component), SiO_2 (representing the Moenkopi Formation and Coconino Sandstone, both quartz-rich rocks), and CaO+MgO+others (representing the

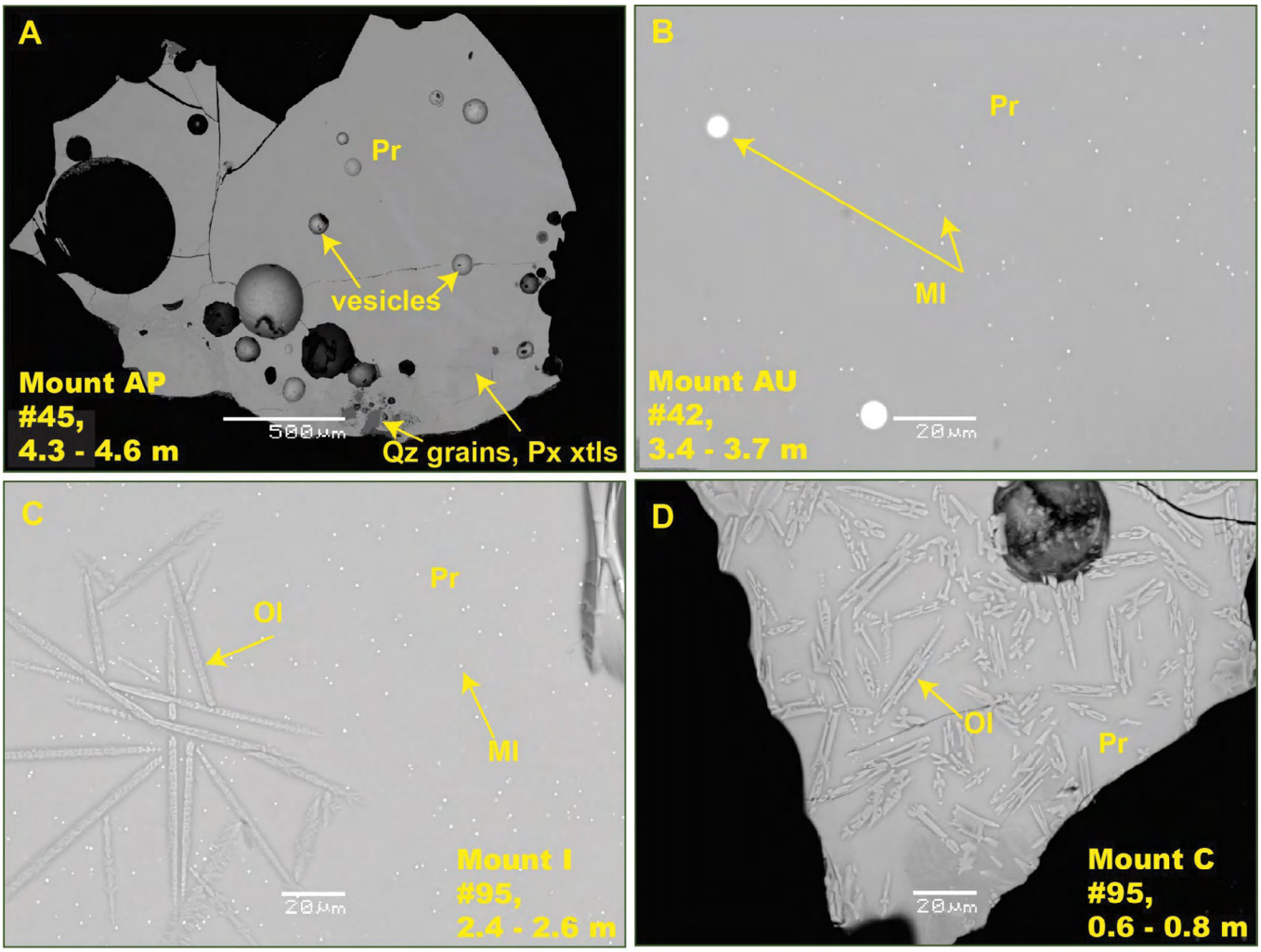

Figure 3. Scanning electron microscope images of pristine glass in impact-melt particles from Meteor Crater. *A*, Mount AP, from drill hole 45, shows a glass particle that is almost completely pristine with no observable submicron metallic inclusions. Near the bottom edge of the image are quartz grains and pyroxene crystals. *B*, Glass in mount AU, from drill hole 42, with micron-scale and submicron-scale metallic inclusions. *C*, Glass in mount I, from drill hole 95, with submicron metallic inclusions and acicular olivine crystals. *D*, Glass in mount C, from drill hole 95, with submicron metallic inclusions and skeletal olivine crystals. Pr, pristine glass; MI, metallic inclusion; Ol, olivine; Px, pyroxene; Qz, quartz.

Table 1. Geochemical compositions, in weight percent, of pristine glass particles from Meteor Crater, measured by wavelength dispersive spectrometry.

[Glass compositions are averages for each mount]

Major-oxide composition	Mount number														
	A	E	G	H	I	J	K	O	P	AC	AD	AG	AL	AP	AQ
SiO_2	52.53	48.80	46.73	48.61	48.00	46.04	46.09	68.20	53.54	49.74	43.53	53.83	44.90	52.55	53.08
Al_2O_3	2.58	4.33	4.51	2.02	2.25	2.66	2.54	7.56	3.11	2.50	2.72	2.05	2.00	3.11	3.15
CaO	13.78	13.41	14.84	8.93	11.62	14.37	13.81	11.47	17.88	13.90	13.98	8.71	9.74	18.12	23.28
MgO	9.38	7.97	7.19	5.70	7.62	8.09	8.72	2.74	12.22	9.64	8.51	5.73	6.54	12.55	16.20
FeO	20.75	23.92	24.41	33.49	28.68	27.68	27.68	6.90	10.22	22.65	29.13	29.62	34.44	11.11	3.94
Na_2O	0.04	0.07	0.07	0.04	0.04	0.05	0.05	0.07	0.05	0.04	0.03	0.04	0.05	0.06	0.06
P_2O_5	0.37	0.42	0.40	0.41	0.38	0.38	0.43	0.03	0.38	0.39	0.38	0.29	0.43	0.39	0.35
K_2O	0.56	0.81	0.66	0.37	0.46	0.42	0.50	1.32	0.72	0.44	0.56	0.40	0.43	0.74	0.75
TiO_2	0.16	0.20	0.32	0.10	0.13	0.19	0.14	0.49	0.18	0.14	0.12	0.10	0.10	0.18	0.17
Cr_2O_3	0.02	0.02	0.02	0.02	0.03	0.03	0.03	0.01	0.02	0.02	0.02	0.02	0.04	0.03	0.02
MnO	0.04	0.05	0.06	0.03	0.03	0.04	0.05	0.06	0.04	0.04	0.04	0.03	0.02	0.05	0.05
NiO	0.60	0.21	0.23	0.13	0.19	0.17	0.13	0.38	0.71	0.10	0.15	0.12	0.14	0.80	0.26
Total	100.80	100.21	99.43	99.86	99.42	100.11	100.15	99.22	99.08	99.59	99.19	100.93	98.82	99.66	101.29

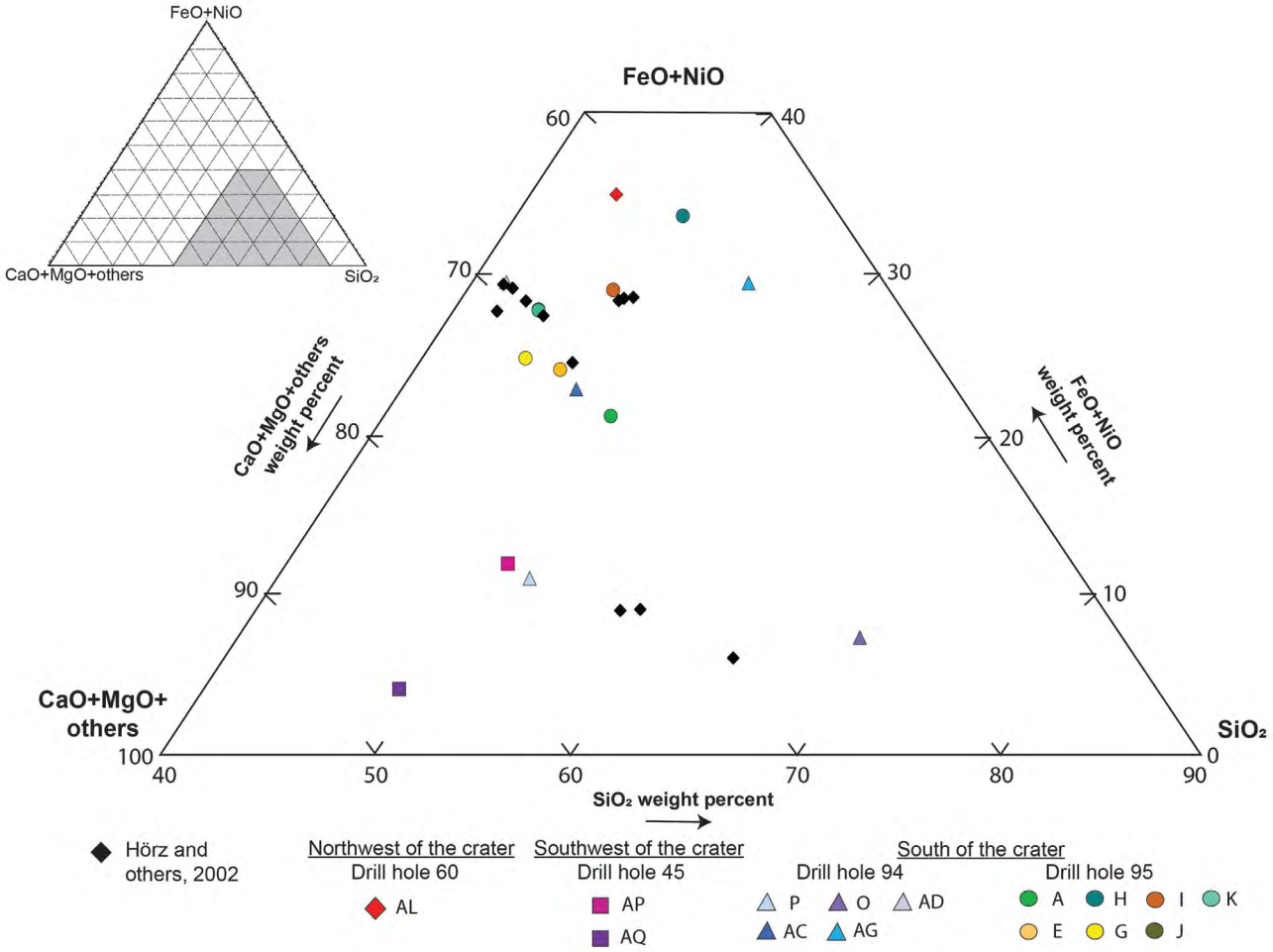

Figure 4. Ternary plot of pristine glass compositions from impact-melt particles at Meteor Crater. Data points are the averaged compositions of pristine glasses from each mount. Colored symbols are the data from this study; black diamonds are Hörz and others (2002), used for comparison. Each symbol type (circle, square, triangle, and diamond) represents the general area within the ejecta blanket these samples were collected from, and color indicates the sample mount. See figure 1 for drill hole locations.

Kaibab Formation's dolomite component). We find that our glasses vary in composition, similar to impact-melt particles analyzed by Hörz and others (2002), who described two distinct compositional groups (a high-Fe and a low-Fe group). Our glasses range in FeO from 3.9 weight percent up to 34.4 weight percent, though still maintaining the compositional "gap" described by Hörz and others (2002) (this "gap" refers to the bimodal distribution of FeO in their samples, where impact melts either have less than 12 weight percent FeO or more than 20 weight percent FeO, and nothing in between). Nearly half of our samples clustered within a few weight percent of each other, ranging from 23 to 29 weight percent FeO. The ejected target rocks are all sedimentary, with ≤2 weight percent FeO (See and others, 2002). Therefore, glasses with high amounts of FeO (referred to as the "high-Fe" group, ≥20 weight percent FeO) indicate a significant contribution from the Canyon Diablo meteorite (Hörz and others, 2002; See and others, 2002). Glasses with lower FeO concentrations typically had higher CaO, MgO, and slightly higher Ni. That is, excluding mount O, averages for low-Fe glasses were 17.7 weight percent CaO, 10.9 weight percent MgO, and 0.5 weight percent NiO, whereas high-Fe glasses were 12.5 weight percent CaO, 7.7 weight percent MgO, and 0.2 weight percent NiO. Silica ranges from 43.5 to 54 weight percent in our glasses, with one anomalous composition (in mount O, which had 68 weight percent SiO_2).

Altered Glass

Texture

Less than half of our samples (40 percent of analyzed samples) had altered (also referred to as "banded") glass, which was low compared to the samples of Hörz and others (2002), in which most glass particles had been hydrated and (or) oxidized. The Hörz and others (2002) study, using samples from the Nininger Collection, analyzed melt beads from the plains surrounding the crater, though exact locations were not recorded. They analyzed 80 particles and noted that only two samples had pristine glass (Hörz and others, 2002), which is not surprising, given that such samples were exposed to the atmosphere and weathering processes for tens of thousands of years. We aimed to limit the amount of weathering that affected our set of samples by sampling from drill cuttings taken deep within the ejecta blanket.

Interestingly, the spatial extent of hydrated samples within our collection was notably variable; there were no obvious trends or correlations between location of impact melt (for example, depth) and alteration. Altered samples were found at a range of depths, spanning from a few inches down to ~9 m below the surface, and both altered and non-altered samples were collected from the same drill hole and depth.

The varieties of banded glass are shown in figure 5. Individual impact-melt fragments are shown in figures 5*A* and 5*B*, where banded glass encompasses the entire outer portion of the fragments, and small amounts of non-altered pristine glass are near the center. Altered glass has also been observed encompassing dendritic pyroxene (fig. 5*C*) and lechatelierite (fig. 5*D*). We did not identify any alteration to pyroxene or olivine, texturally or compositionally.

Compositional Data

We carried out WDS measurements on altered glass for individual fragments within two impact-melt particles. The altered-glass oxide totals were ~82–94 percent, compared to pristine glass totals of ~98–101 percent (totals that were outside of this range were not used in the data analysis). The altered glass had a noticeable enrichment in SiO_2: pristine glasses typically ranged from ~44 to 54 weight percent, however, the averaged altered glass within individual fragments spanned from 52 to 66 weight percent. When normalized to 100 for direct comparison to pristine glasses, this average altered glass value increases to ~62–73 weight percent SiO_2. There was no noticeable difference in Fe content, but a depletion in both MgO and CaO and an enrichment in Al_2O_3 were observed in the altered glass.

Crystalline Groundmass

Texture

The majority of crystalline groundmass in the impact-melt particles is calcium-rich pyroxene and lesser amounts of olivine— both varying in Mg to Fe concentrations. Olivine was observed as euhedral or subhedral crystals with dark cores (higher Mg) and bright rims (higher Fe; fig. 6*A*), skeletal (fig. 6*B*), and acicular in habit (fig. 3*C*). Individual olivine crystals are readily identifiable in all samples, with sharp and well-defined edges.

Pyroxene is much more variable in texture than olivine. The SEM images in figure 6*C*,*D* show examples of an impact-melt particle that has no detectable glass and is completely crystalline, with both pyroxene and olivine crystals and numerous rock fragments and metallic spherules. Figure 6*A* is a close-up of the crystalline groundmass, with euhedral to subhedral olivine surrounded by and included in anhedral pyroxene. Another example of this textural relationship is illustrated in figure 6*B*, which shows a granular pyroxene crystal encroaching on acicular skeletal olivine in the lower left corner of the image. Submicron metallic inclusions are present in both pristine glass and the feathery pyroxene figure 6*E*. A thin, ~1-micron (μm)-wide, semi-fuzzy bright rim outlines many of the individual crystals in this image. The brightness of the rim is the result of a higher concentration of iron compared to the crystal's core. We were able to qualitatively confirm this with EDS; however, because the thickness of the rim is essentially the diameter of the beam size on the SEM, we were unable to quantitatively characterize this compositional change due to the beam picking up peripheral phases.

The last impact-melt fragment included in this set of SEM images (fig. 6*F*) is composed entirely of pyroxene (except for a carbonate inclusion near the center of the image). Interestingly, this particle displays three crystal habits, referred to as habit 1, 2, and 3 (fig. 6*F*). Habit 1 crystals are sub- to anhedral, with only the slightest thin bright rim, and are located on the left side of the fragment. The crystal edges are sharp, well-defined, and surrounded by a very minor/thin matrix of assumed glass (areas are too small to analyze and

confirm). Habit 2 is in the lower right corner of the image and comprises anhedral crystals that can be identified by their fuzzy bright rims. There is no interstitial space between these crystals. Habit 3 is characterized by small, dendritic pyroxene crystals. Habit 3 overprints habit 2. There is a clear boundary between habit 1 and 3, but the transition between 2 and 3 is gradational. Remnants of the fuzzy bright rims of habit 2 are still visible, though the dendritic habit spans both cores and rims of the former habit 2 crystals.

Compositional Data: Pyroxene

While imaging and characterizing our samples, we often used EDS on the SEM for spot checks to confirm mineral phases. We took full spectral profiles of 12 pyroxene crystals to characterize the range of compositions. Table 2 shows measured pyroxene compositions, and figure 7 are those data points plotted on a ternary diagram. The majority of the pyroxene is augite, with a few crystals having slightly higher calcium.

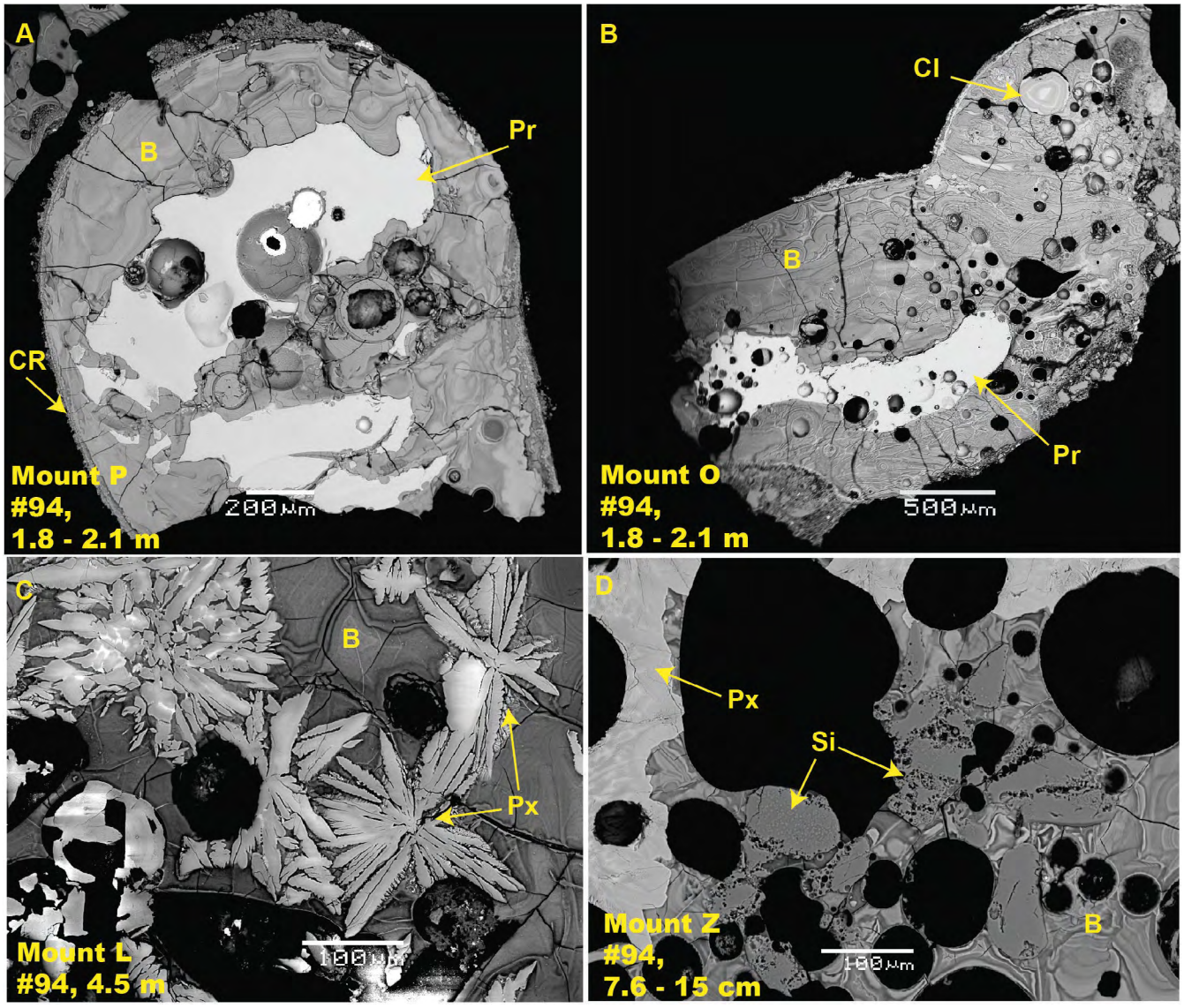

Figure 5. Scanning electron microscope images of banded (altered) glass. *A*, Image of mount P, from drill hole 94. Banded glass is along the outer portion of this fragment, with pristine glass in the center. There is a carbonate rind along most of the rim. *B*, A fragment from mount O, drill hole 94, that mostly consists of banded glass, though a small region in the center is still pristine and has not been altered. *C*, Dendritic pyroxene within banded glass, mount L, drill hole 94. *D*, Banded glass with fragments of lechatelierite (labeled "Si" in the figure) and pyroxene groundmass in the upper portion of the melt fragment, mount Z, drill hole 94. Several of the lechatelierite fragments have small crystals in the center of the particles, indicating some recrystallization prior to complete solidification. Pr, pristine glass; B, banded glass; Cl, carbonate inclusions; CR, carbonate rind; Si, silica phase; Px, pyroxene.

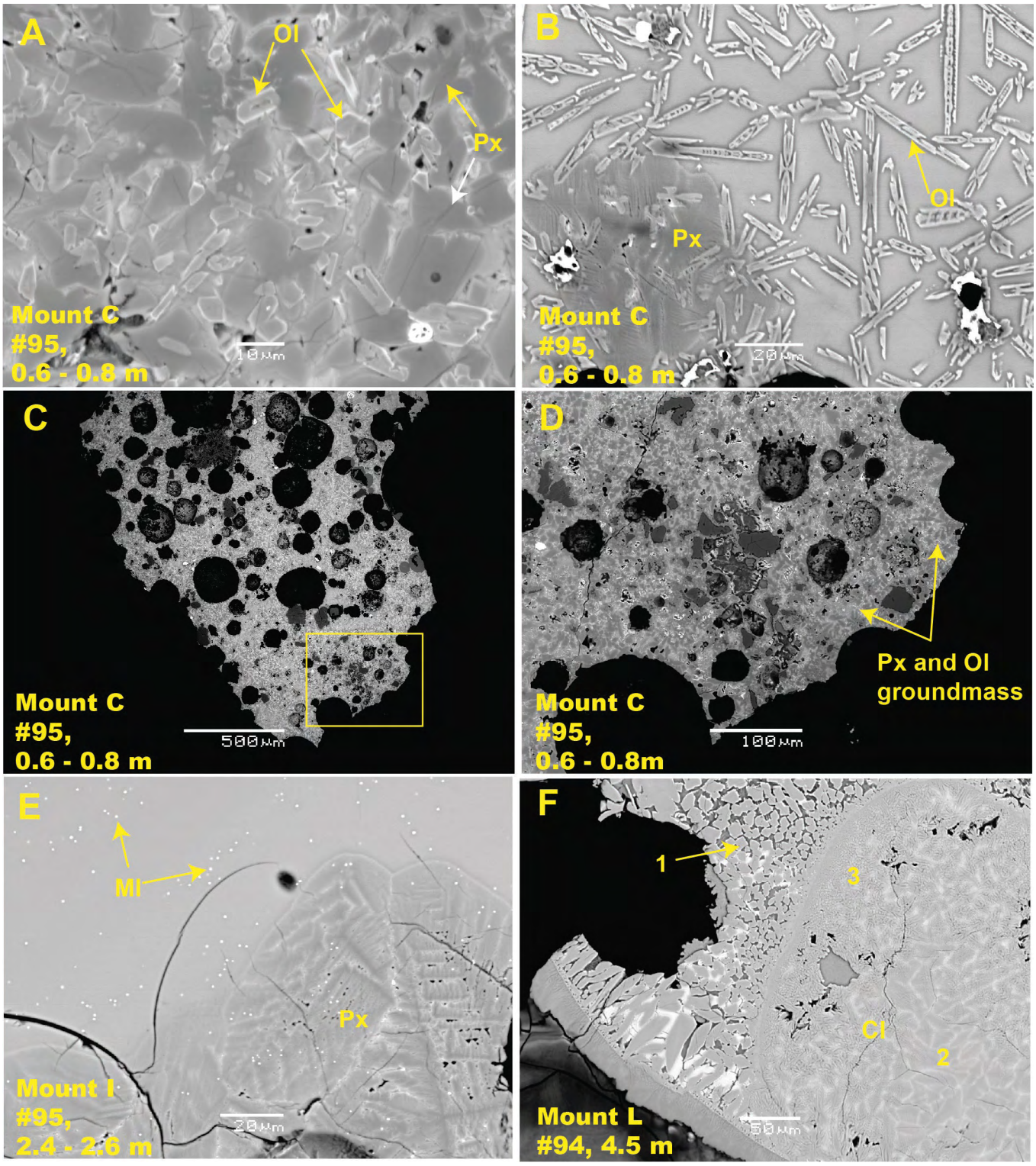

Figure 6. Scanning electron microscope images of pyroxene and olivine within impact-melt fragments in three different mounts from drill hole 95. *A*, In mount C, olivine crystals have bright rims and slightly darker cores; pyroxene crystals are dark. *B*, In mount C, darker mass in lower left corner is pyroxene groundmass; skeletal crystals are olivine. *C*, A fully crystalline impact-melt fragment in mount C. *D*, Inset in image C showing the fine-grained crystalline groundmass that is typical for many impact melts sampled at Meteor Crater. *E*, Pristine glass with submicron metallic inclusions (upper part of image) in mount I; lower part of image shows feathery anhedral pyroxene groundmass. *F*, Apart from the carbonate inclusion near center of image, the entire fragment in mount L is composed of different textural pyroxene groups or clusters. Numbers 1, 2, and 3 refer to the different habits of pyroxene observed; these are discussed in text. Cl, carbonate inclusion; MI, metallic inclusion; Ol, olivine; Px, pyroxene.

Table 2. Geochemical compositions, in weight percent, of pyroxene within impact-melt particles from Meteor Crater, measured by energy dispersive X-ray spectrometry.

[Capital letter refers to the sample mount, and *gr* refers to the grain number that was analyzed]

Major-oxide composition	Sample mount and grain number										
	I, gr3	L, gr1	M, gr2	M, gr4	M, gr4	AJ, gr2	An, gr1	AO, gr5	AO, gr5	AO, gr5	AU, gr1
SiO_2	49.43	50.94	53.62	45.80	60.20	51.88	51.86	53.41	54.24	50.47	47.77
Al_2O_3	2.60	3.16	2.47	2.45	2.89	1.02	1.20	2.75	0.43	3.44	2.37
MgO	28.74	16.82	12.32	15.25	13.53	14.39	16.82	17.20	19.02	4.44	11.30
FeO	1.05	5.11	11.72	14.45	3.56	15.90	17.77	0.61	9.01	28.34	19.80
CaO	17.58	23.71	18.66	20.84	18.47	16.10	11.61	25.23	16.36	11.81	17.44
MnO	0.33	0.01	0.00	0.41	0.08	0.00	0.03	0.00	0.10	0.00	0.00
TiO2	0.00	0.21	0.27	0.29	0.47	0.19	0.12	0.25	0.06	0.16	0.45
Cr_2O_3	0.14	0.18	0.00	0.16	0.00	0.00	0.00	0.23	0.03	0.03	0.00
Na_2O	0.00	0.00	0.03	0.03	0.00	0.00	0.11	0.00	0.00	0.00	0.04
K_2O	0.00	0.00	0.58	0.00	0.80	0.00	0.00	0.01	0.01	0.68	0.00
NiO	0.53	0.47	0.38	0.44	0.36	0.28	0.61	0.03	0.78	0.11	0.11
Total	100.40	100.61	100.05	100.12	100.36	100.39	100.37	99.98	100.31	100.15	100.10

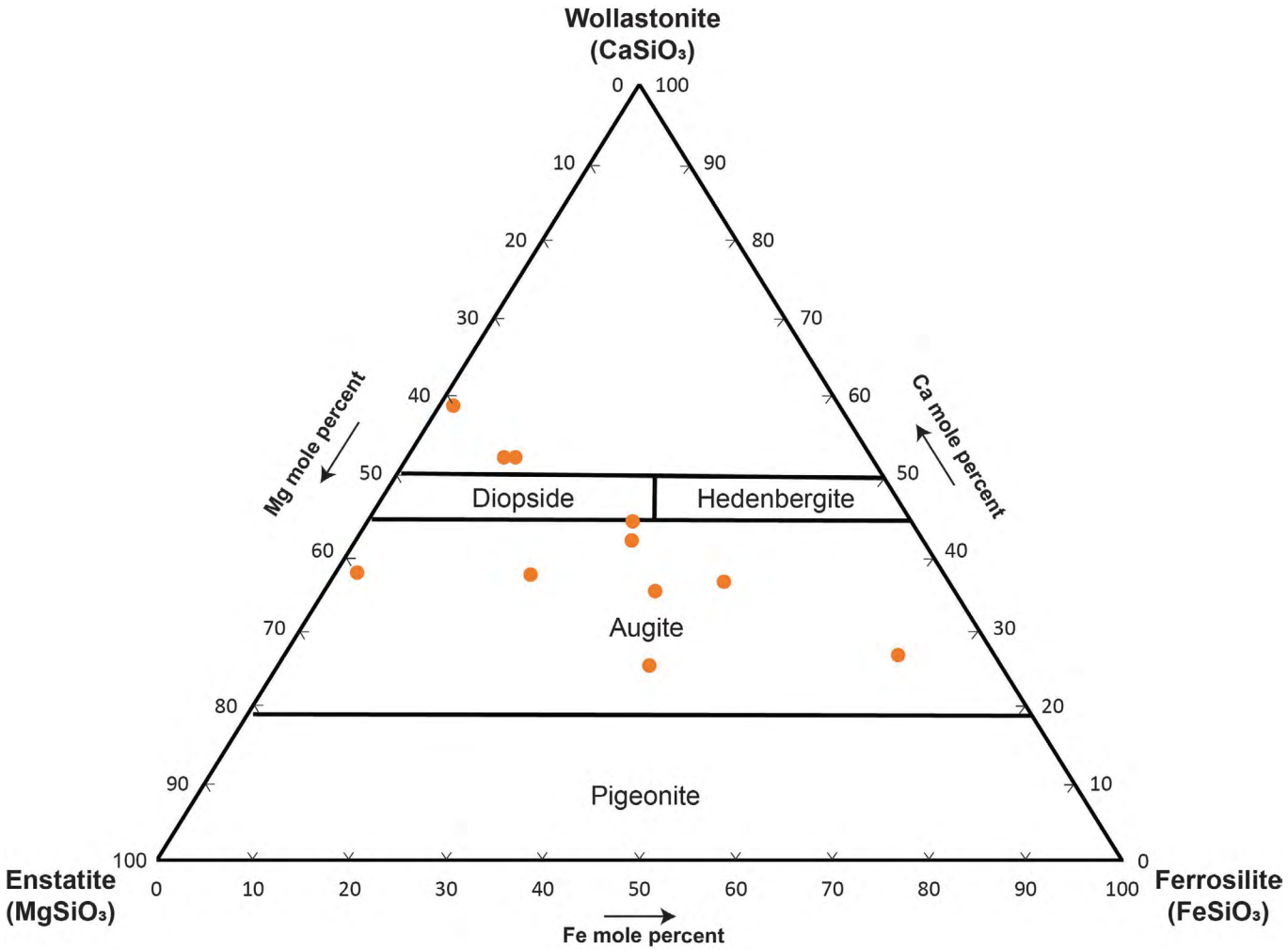

Figure 7. Ternary diagram of pyroxene compositions in impact-melt fragments from Meteor Crater as analyzed by energy dispersive X-ray spectrometry.

Compositional Data: Olivine

We collected ten full spectral analyses on olivine crystals using EDS (table 3). Most of the olivine crystals tended to be rich in iron (fig. 8). One sample (mount AQ) had a population of olivine that was almost purely forsteritic. This olivine population had <5 weight percent FeO, whereas most olivine in our sample set ranged from 34 to 56 weight percent FeO.

Carbonate Inclusions

Texture

Carbonate inclusions (CIs) are common in most of our impact-melt particles. They average ~1.4 modal percent of the samples and come in a range of different sizes, shapes, and compositions (fig. 9). Sizes range from <20 µm to >200 µm in diameter. CIs can be rounded or subrounded, and some were deformed by the growth of crystals in the impact melt. For example, in figure 9*B*, the right side of the carbonate inclusion is being deformed from the growth of granular pyroxene. We also observed compositional bands with different concentrations of MgO and CaO. Examples are shown in figure *9A–C*: figure 9*A* shows CIs with concentric bands of pyroxene (light bands have higher CaO and dark bands have higher MgO), figure 9*B* shows euhedral calcite crystals within the inclusion, and 9*C* shows euhedral calcite crystals with compositional zoning in one of the CIs. CIs can be individual blebs (as shown in fig. 9*C*) or connected, with some displaying a budding texture (fig. 9*D*). Barium sulfate is associated with many CIs and is often found as rims around the carbonate blebs or as tabular euhedral inclusions within the blebs (fig. 9*A,C,E,F*). In our samples, CIs are also found among partially melted lithics (fig. 10*A–D*). Figure 10*A* shows

Table 3. Geochemical compositions, in weight percent, of olivine within impact-melt particles from Meteor Crater, measured by energy dispersive X-ray spectrometry.

[Capital letter refers to the sample mount, and *gr* refers to the grain number that was analyzed]

Major-oxide composition	Sample mount and grain number									
	I, gr1	J, gr1	AM, gr1	AM, gr6	AQ, gr4	AU, gr1	AV, gr1	AV, gr1	AV, gr3	AW, gr1
SiO_2	43.80	35.41	38.77	30.91	41.01	35.59	37.90	35.92	37.62	32.39
Al_2O_3	1.24	0.23	1.01	0.00	0.00	2.44	1.30	0.00	0.17	0.15
MgO	13.63	20.92	13.59	10.77	49.63	11.99	16.08	23.12	25.03	14.84
FeO	34.14	38.39	42.63	56.63	3.31	35.44	42.80	37.57	35.27	47.34
CaO	6.12	3.86	2.20	1.67	5.48	10.74	1.19	2.14	1.26	3.38
MnO	0.00	0.16	0.00	0.03	0.03	0.00	0.08	0.14	0.25	0.08
TiO_2	0.21	0.17	0.25	0.00	0.02	0.05	0.26	0.03	0.00	0.19
SO_3	0.00	0.00	0.31	0.17	0.14	0.78	0.15	0.00	0.11	0.00
Na_2O	0.07	0.08	0.00	0.00	0.00	0.03	0.05	0.00	0.00	0.03
K_2O	0.4	0.06	0.00	0.00	0.00	0.35	0.00	0.00	0.00	0.31
NiO	0.34	0.54	0.61	0.20	0.98	0.51	0.03	1.45	0.68	1.08
Total	100.05	100.00	100.21	100.44	100.66	100.22	100.06	100.66	100.65	100.03

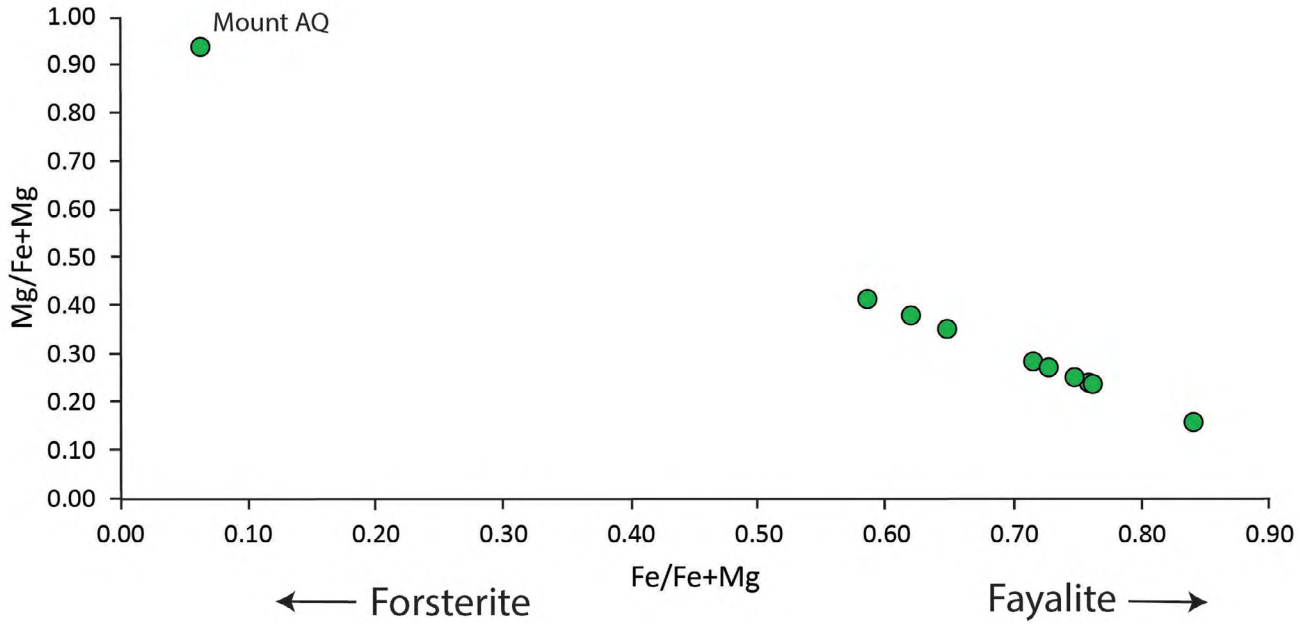

Figure 8. Plot showing magnesium versus iron concentrations in olivine crystals in impact-melt fragments. Olivine trending to the right is fayalitic and to the left forsteritic.

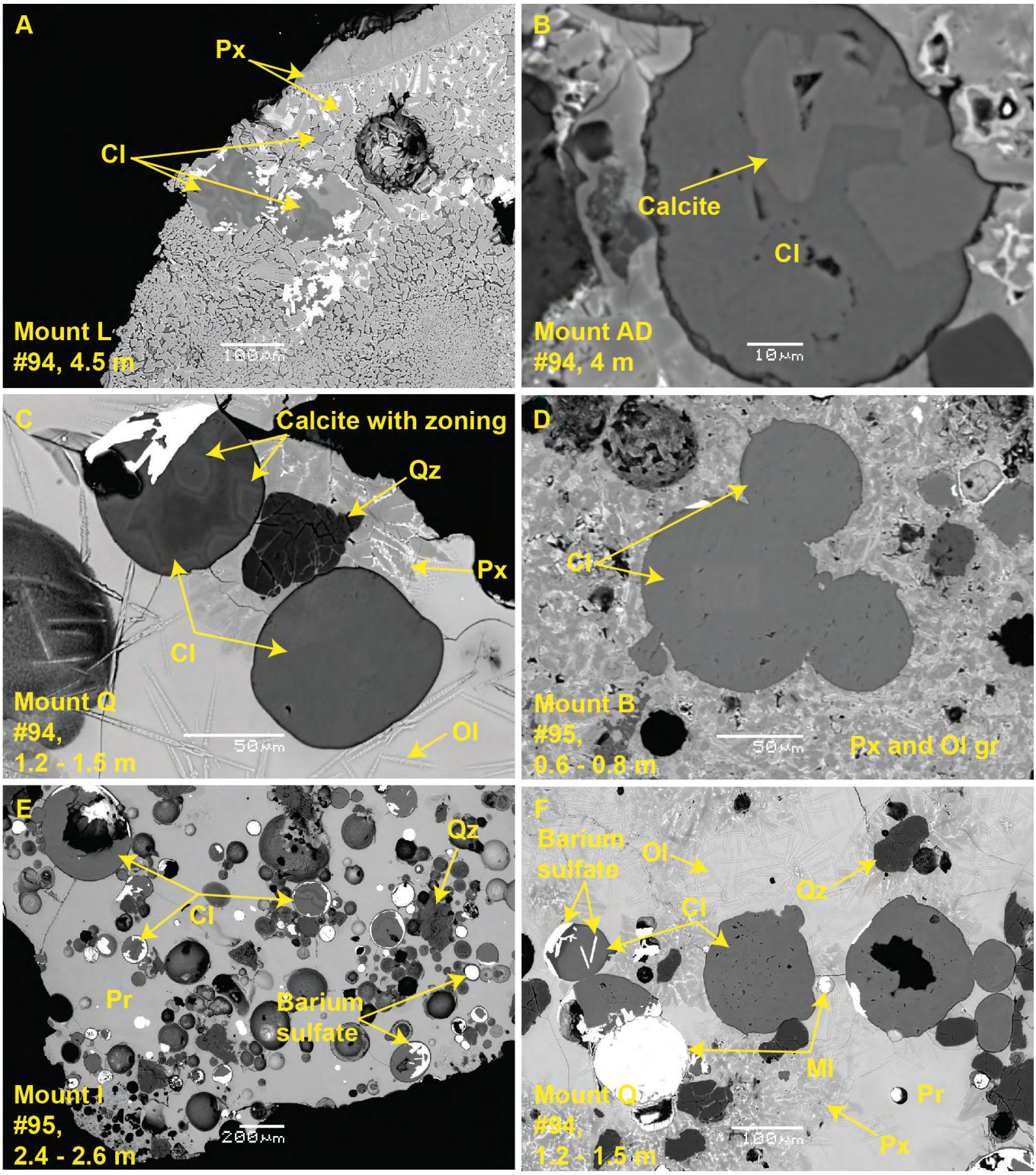

Figure 9. Scanning electron microscope (SEM) images of carbonate inclusions (CIs) in impact-melt fragments from drill holes at Meteor Crater, Arizona. *A*, Fragment from mount L, drill hole 94, is almost completely composed of pyroxene, with several CIs incorporated within the pyroxene crystals. Bright phases in the carbonates are barium sulfate. *B*, Large CI in mount AD, from drill hole 94, with visible calcite crystals, notably a large euhedral crystal near the center. The matrix of the CI has slightly higher magnesium content than the euhedral crystals, allowing individual calcite crystals to be visible in the SEM image. *C*, Two CIs in mount Q, from drill hole 94. One has visible calcite crystals and zonation and the other is completely homogeneous in composition. *D*, In mount B, from drill hole 95, CIs are surrounded by granular pyroxene and olivine groundmass. Carbonates have a budding texture. *E*, Mount I, from drill hole 95, has numerous CIs within a pristine glass sample. Barium sulfate inclusions are common in most CIs. *F*, Mount Q, from drill hole 94, has multiple CIs, some with barium sulfate inclusions. CIs in this sample are within pristine glass alongside acicular olivine and patches of granular pyroxene. Two metallic inclusions are also present. Pr, pristine glass; MI, metallic inclusion; Ol, olivine; Px, pyroxene; Px and Ol gr, pyroxene and olivine groundmass; Qz, quartz.

a partially melted quartz-rich lithic with CIs both incorporated within and surrounding this clast; figure 10*B* shows a partially melted Kaibab Formation lithic fragment with dolomite and quartz grains in the upper half of the image and CIs in the lower half, surrounded by granular pyroxene. Figure 10*C* shows another partially melted lithic fragment with CIs, and figure 10*D* shows a carbonate matrix with dolomite grains as inclusions.

Compositional data

CIs are calcium rich with lesser amounts of magnesium (concentrations range from 1 to 21 weight percent MgO, though the mean value is 4.3 weight percent and the median value is 3.4 weight percent MgO), and trace to minor amounts of SiO_2, Al_2O_3, FeO, and NiO (averages of 0.14, 0.04, 0.37, and 0.03 weight percent, respectively). Figure 11 compares MgO and CaO concentrations of CIs, a carbonate rind coating one impact-melt particle, and Kaibab Formation lithics. Several CIs plot near Kaibab Formation compositions, having a similar CaO to MgO ratio. CIs plot on a linear trend line, decreasing in magnesium as calcium concentrations increase. The carbonate rind composition is on this trend line, with an average of 50.2 weight percent CaO and 3.44 weight percent MgO. One slight difference in composition between CIs and the carbonate rind are concentrations of SiO_2 and Al_2O_3. The difference is minor, but most CIs have <0.2 weight percent SiO_2, whereas the rind ranges from 0.6 to 1.3 weight percent. Content of Al_2O_3 in CIs is typically <0.05 weight percent and the rind ranges from 0.1 weight percent to 0.5 weight percent (fig. 12).

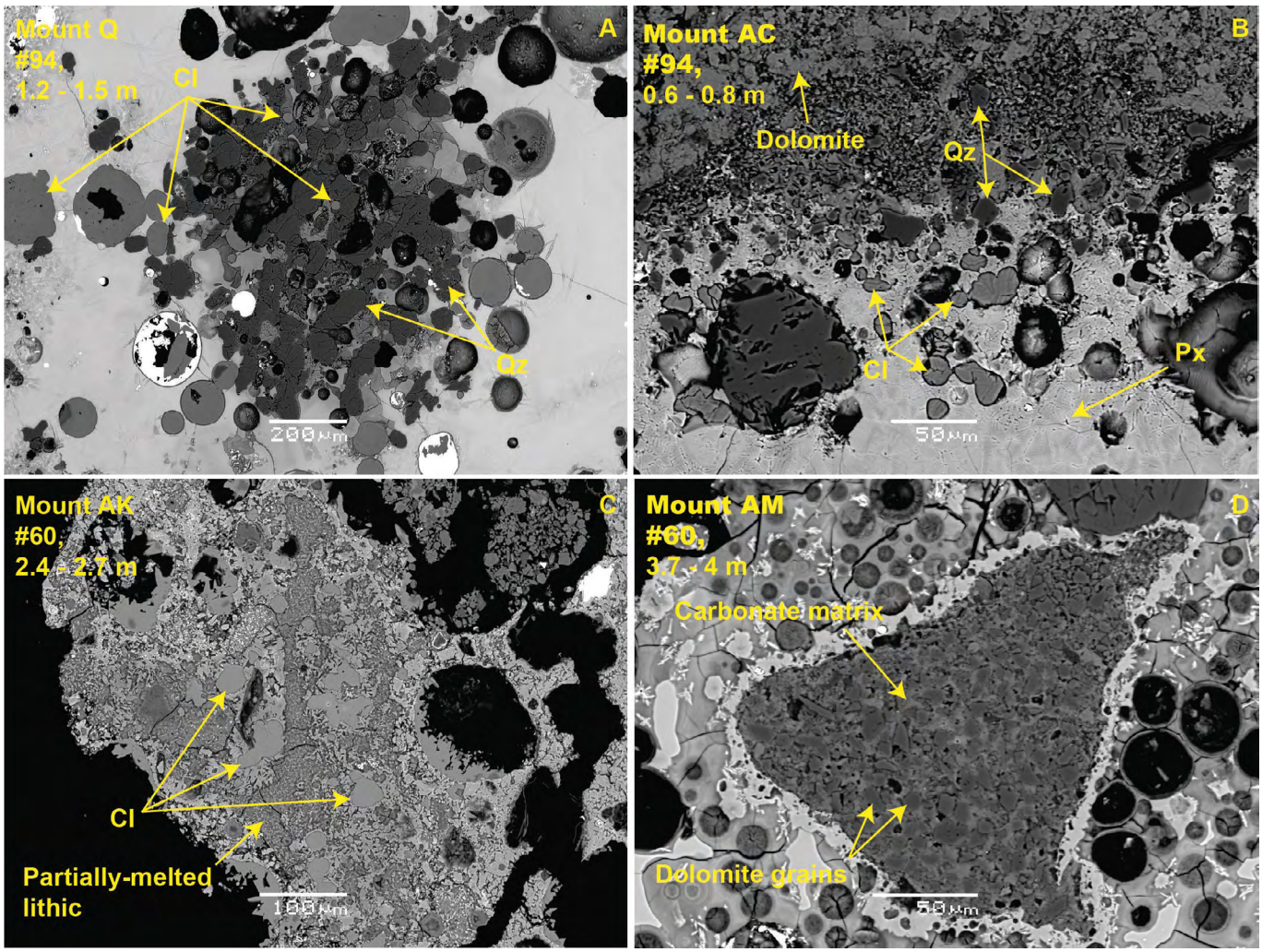

Figure 10. Scanning electron microscope images of impact-melt fragments from Meteor Crater showing carbonate inclusions associated with partially melted lithic grains. *A*, Multiple carbonate inclusions incorporated within and surrounding this quartz-rich, partially melted lithic in mount Q, from drill hole 94. *B*, Partially melted Kaibab Formation lithic fragment in mount AC, from drill hole 94, with dolomite and quartz grains in the upper half of the image and carbonate inclusions in the lower half of the image, surrounded by granular pyroxene groundmass. *C*, Partially melted lithic with carbonate inclusions in mount AK, from drill hole 60. *D*, Dolomite grains within an extensive carbonate matrix in mount AM from drill hole 60. CI, carbonate inclusion; Px, pyroxene; Qz, quartz.

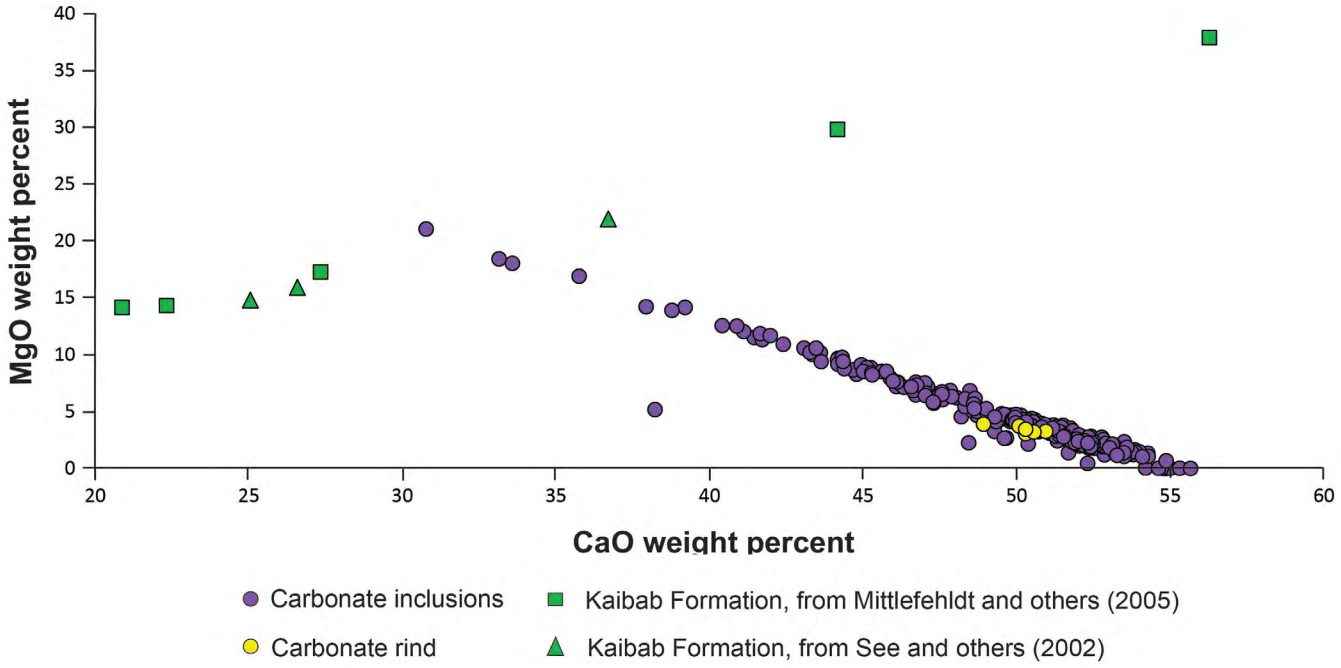

Figure 11. Plot of CaO versus MgO, in weight percent, in carbonate inclusions and carbonate rind in impact-melt fragments from Meteor Crater, Arizona. Compositions of Kaibab Formation clasts from See and others (2002) and Mittlefehldt and others (2005) are included for reference.

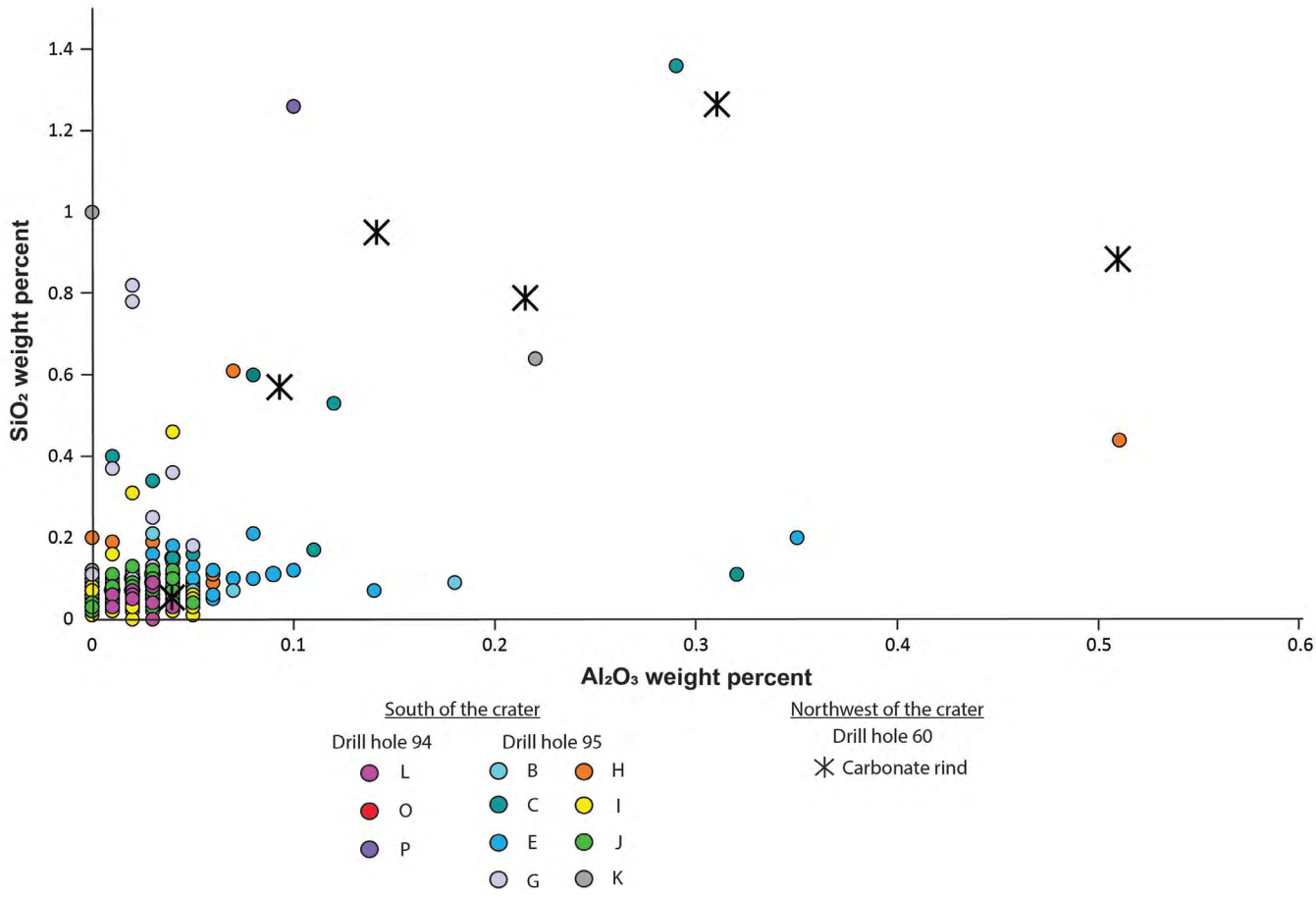

Figure 12. Plot of Al_2O_3 versus SiO_2, in weight percent, in carbonate inclusions and carbonate rinds in impact-melt fragments from Meteor Crater, Arizona.

Barium Sulfate

Texture

Barium sulfate is common in most impact-melt samples, either as individual spherules or associated with carbonate inclusions (as described above). When found with carbonates, barium sulfate takes the form of elongated tabular crystals within the CIs or as rims surrounding the carbonates (fig. 9*A,C,E,F*). Crystals range from <20 µm to ~100 µm and are often euhedral to subhedral. When found as rims, they do not always completely surround the CIs nor are they of uniform thickness. The BSE images results show individual barium sulfate spherules are bright, rounded to semi-rounded in shape, often appearing similar to metallic inclusions (fig. 9*E,F*).

Compositional Data

Inclusions within CIs and individual spherules were analyzed within two impact-melt particles (table 4). Minor compositional variations do exist, though barium sulfate is generally homogeneous throughout the samples, both as spherules and inclusions. Major oxides BaO and SO_2 range from ~61 to 65.5 weight percent and 32.5 to 35 weight percent, respectively. BaO and the minor oxide SrO have an inverse relationship, where higher concentrations of strontium lead to lower amounts of barium. Variation in CaO was the main compositional difference between barium sulfate inclusions and spherules. The change is slight, but there is a small increase in CaO when barium sulfate is found within CIs. As individual spherules, CaO ranges from >0.1 to 0.25 weight percent (with two outliers of 0.4 and 0.7 weight percent CaO), and as inclusions from 0.25 to 1.4 weight percent. It should be noted that the outliers are located within a few microns of CIs.

Silica

Textures

Without using Raman spectroscopy or another technique for silica polymorph identification (as in Kingma and Hemley, 1994), it is difficult to determine which phase was observed in the samples. In figure 13, we have highlighted some of the observed textures, ranging from fractured to amorphous glass.

Fractured quartz grains that did not encounter high enough pressures and temperatures to cause melting are common in the impact-melt particles at Meteor Crater. Figure 13*A* shows an example of several fractured quartz grains surrounding a potassium feldspar crystal. The matrix of the particle is granular pyroxene, olivine, and high-Z (mean atomic number) material. Much of the high-Z material had higher concentrations of iron compared to surrounding phases (causing the high-Z material to appear brighter), though it was typically too small to characterize. We also observed silica grains with rims of either small silica aggregates or crystallized silica nucleating

Table 4. Geochemical compositions, in weight percent, of barium sulfate spherules and inclusions within impact-melt particles from Meteor Crater, measured by wavelength dispersive spectrometry.

[*gr#_#* refers to the grain number and the numbered analysis; *s* and *i* (spherule and inclusion, respectively) refers to the phase's form]

Major-oxide composition	Sample mount AD										Sample mount AG					
	gr5_1,*i*	gr5_2,*s*	gr5_4,*i*	gr8_1,*i*	gr8_2,*s*	gr8_3,*i*	gr8_4,*s*	gr8_5,*s*	gr8_6,*i*	gr9_1,*i*	gr9_2,*i*	gr9_3,*s*	gr9_4,*i*	gr1_1,*s*	gr1_3,*s*	gr1_5,*s*	gr3_1,*s*	gr3_2,*s*	gr3_3,*i*
SO_2	34.26	32.68	33.88	33.51	33.38	33.26	35.03	34.09	34.91	32.58	34.60	33.78	34.26	34.3	34.15	33.93	33.46	33.86	33.13
CaO	1.37	0.12	0.69	0.31	0.74	0.49	0.42	0.15	0.32	0.27	0.45	0.17	0.28	0.04	0.16	0.07	0.09	0.11	0.31
SrO	0.52	0.41	0.42	0.92	0.58	2.11	3.31	2.96	2.30	0.71	0.51	2.49	0.51	0.30	0.62	1.52	1.59	0.37	0.06
BaO	63.38	65.12	63.84	64.29	63.74	62.57	60.84	61.99	62.20	64.78	65.10	62.63	63.59	65.03	64.25	63.84	63.63	65.16	65.36
Total	99.52	98.34	99.83	99.03	98.44	98.43	99.59	99.18	99.63	98.34	100.65	99.07	98.63	99.67	99.19	99.36	98.77	99.5	98.86

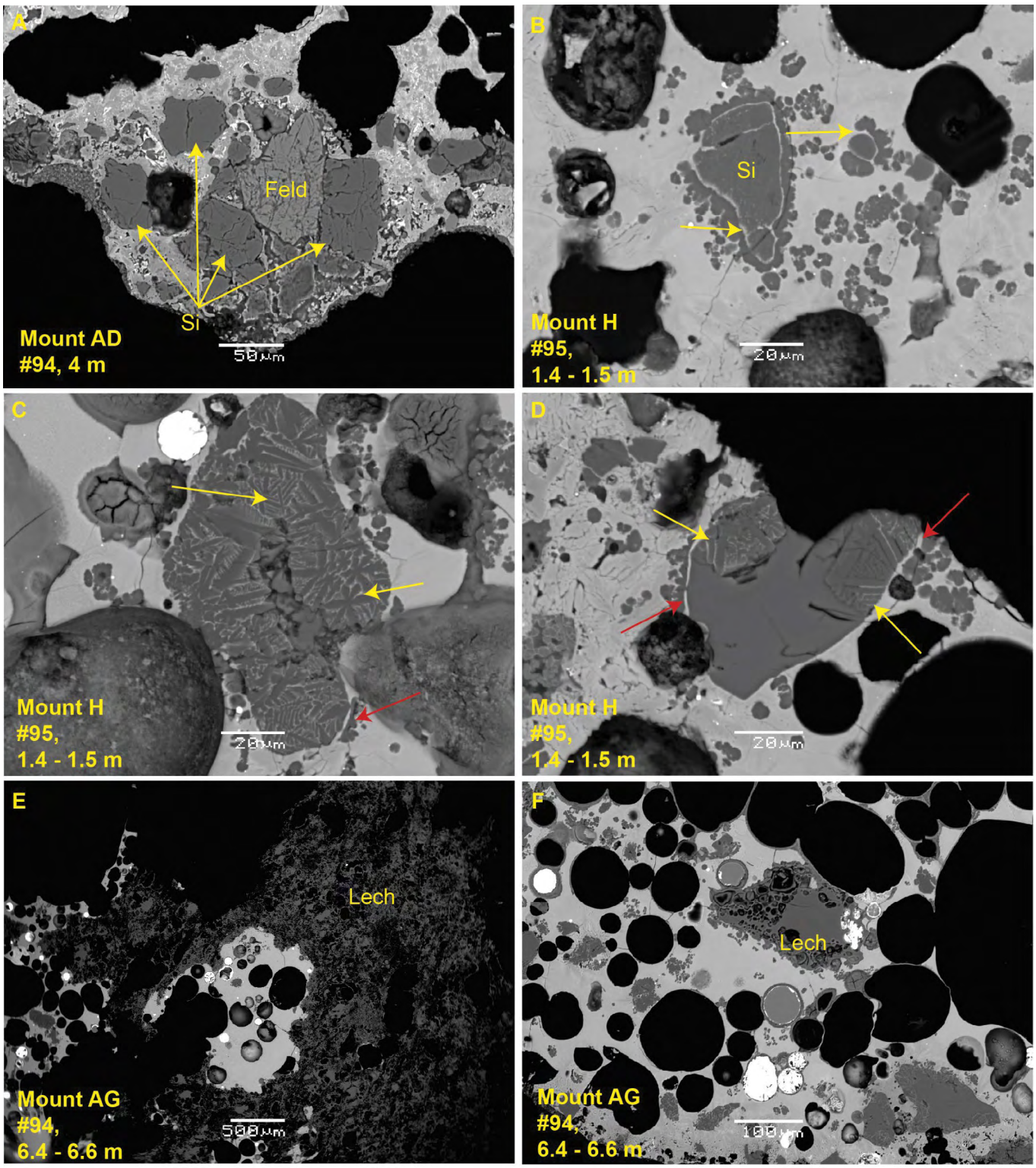

Figure 13. Scanning electron microscope images of silica phase textures in impact-melt fragments from Meteor Crater, Arizona. *A*, In mount AD, from drill hole 94, a cluster of fractured silica grains surround a potassium feldspar fragment, which are all encased in granular pyroxene and olivine groundmass. *B*, Large silica grain with recrystallized rim from mount H, drill hole 95. Similar texture is around a smaller, semi-rounded grain to the right. Yellow arrows point to the boundaries between grains and rims. *C*, Fully recrystallized silica in mount H. Grain shows numerous skeletal dendritic habits, with higher-Z material within the void spaces (indicated by yellow arrows). Red arrow points to growth rim. *D*, Partly recrystallized silica in mount H, with similar habit to *C* on the edges of the grain. Yellow arrows point to higher-Z material surrounding the silica crystal habit; red arrows point to growth rims. *E*, Particle in mount AG, from drill hole 94, almost fully composed of lechatelierite and minor amounts of impact melt. *F*, Small lechatelierite fragment within an impact-melt particle in mount AG. Feld, feldspar; Lech, lechatelierite; Si, silica.

from the edges of the larger grains (fig. 13*B*). Typically, there is a distinct thin boundary between the interior grain and the rim that is composed of higher-Z material (or impact melt) compared to the silica, though it is too narrow for analysis. Another example is a smaller, semi-rounded grain (to the right of the larger silica grain in fig. 13*B*) that has a thin boundary between the interior grain and a partial rim. Populations of recrystallized or partially recrystallized silica are shown in figure 13*C,D*. Skeletal dendritic habits with higher-Z material surrounding the lamellar structure are observed throughout the silica particle in figure 13*C* and along the edges of the grain in figure 13*D* (yellow arrows). Semi-rounded growth rims (similar to those in fig. 13*B*) are present in a few locations around both silica particles (red arrows). Lechatelierite is also found in many of our samples of impact melts. Some particles are almost fully composed of lechatelierite with only minor amounts of melt present (fig. 13*E*), or as small fragments in melt-rich particles (fig. 13*F*).

Metallic Inclusions

Texture

Metallic inclusions (MIs) are small (submicron to ~250 µm in diameter), rounded, subrounded, or irregular in shape and are incorporated into impact-melt particles. MIs should not be confused with metallic spheroids described in previous work (for example, Mead and others, 1965), which are individual spheres typically composed of an iron-nickel metallic core coated with a layer of gray iron oxide and a thin outer layer of siliceous glass. MIs are similar to impactite metallic particles described by Kelly and others (1974), though with slight differences (described below).

Most MIs have three distinct phases, which we describe as bright, intermediate, and dark (fig. 14). The bright phase is the most common and abundant of the three and has a recrystallized skeletal texture (Vdovykin, 1973). The matrix of the MIs, encapsulating the bright phase, is the intermediate phase. The dark phase is the least common and is not always observed in the MIs. When present, it is often irregular in shape and can be found as part of the matrix or as inclusions within the bright phase.

Compositional data

The three phases described above—bright, intermediate, and dark—all have distinct compositions (fig. 15). The bright phase is an Fe-Ni metal, where the nickel ranges from ~13 to 75 weight percent and iron ranges from 22 to 84 weight percent. The intermediate phase is (Fe, Ni)S, all elements having similar concentrations. The dark phase is predominately Fe-Ni (15–60 percent and 6–55 percent, respectively), with minor amounts of silica and another element that was not identified. Based on previous work (for example, Mead and others, 1965; Kelly and others, 1974) it is likely this unidentified phase is a Fe-Ni phosphide; however, we did not calibrate the electron microprobe for phosphorous when analyzing these samples and therefore this phase resulted in low totals.

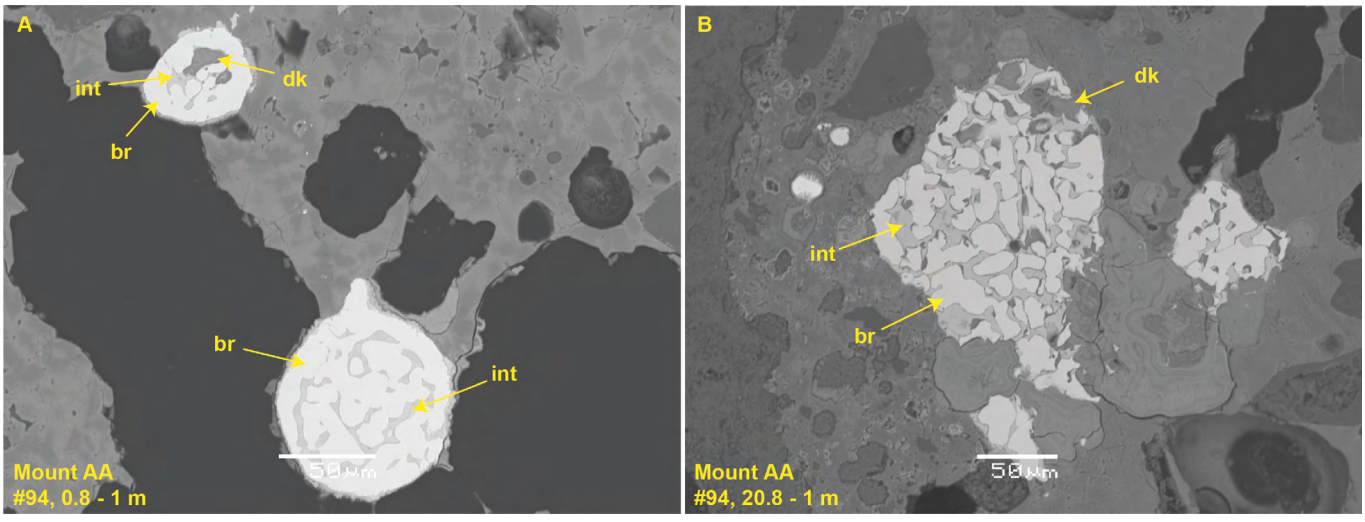

Figure 14. Scanning electron microscope images of metallic inclusions in impact-melt particles from Meteor Crater, Arizona. *A,* Two subrounded metallic inclusions in mount AA. Metallic inclusion in upper left is made up of all three phases (bright, intermediate, and dark); metallic inclusion near bottom of image is composed of only the bright skeletal phase surrounded by the intermediate phase. *B,* An irregular-shaped metallic inclusion in mount AA composed of all three phases. br, bright phase; dk, dark phase; int, intermediate phase.

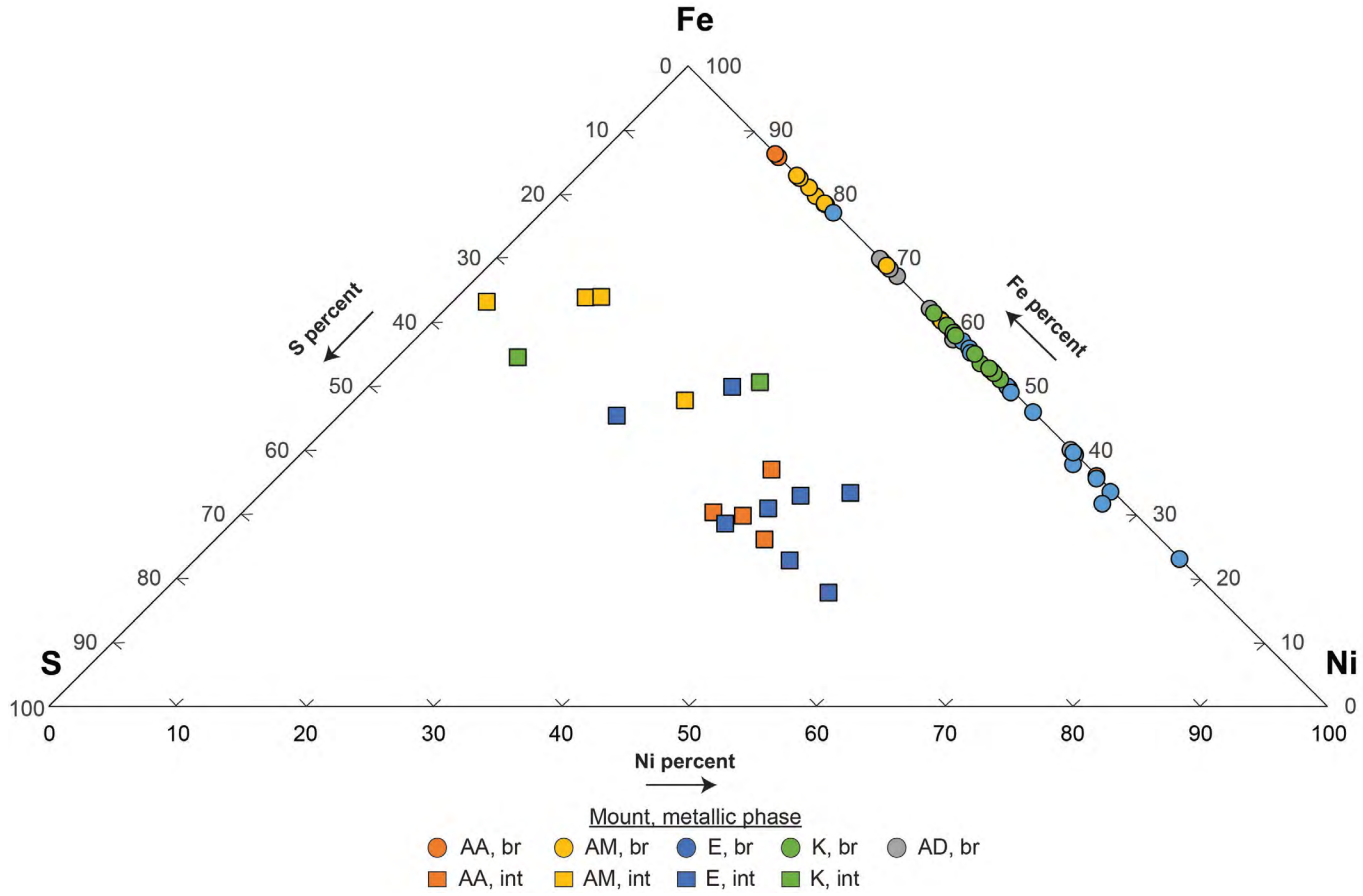

Figure 15. Iron-nickel-sulfur ternary diagram for the bright and intermediate phases within metallic inclusions in impact-melt fragments at Meteor Crater, Arizona. Circles are bright phases and squares are intermediate phases. We did not include the dark phase here because of low microprobe totals. br, bright phase; int, intermediate phase.

Discussion and Summary

Alteration and Pristine Glass

Hydrated/altered impact-melt particles analyzed by previous researchers (for example, Hörz and others, 2002) were common, therefore it was surprising to find that nearly 75 percent of our analyzed melts had measurable amounts of pristine glass. Pristine glass compositions resembled a trend identified by Hörz and others (2002), where a distinct compositional "gap" was observed in Fe concentrations. Pristine glasses could be categorized into a "low Fe" (<12 weight percent FeO) group or a "high Fe" (>20 weight percent FeO) group. Target rocks at Meteor Crater are all low in Fe content (<2 weight percent FeO, See and others, 2002), indicating that a significant contribution of Fe from the meteorite was incorporated into the impact melts (Hörz and others, 2002).

Altered glass was identified in ~40 percent of our impact-melt particles. Interestingly, alteration of impact melts appears to be spatially non-uniform. We found that both altered and non-altered samples were present in sample bags from the same drill holes and depth, suggesting no spatial trend or correlation between the location of the impact melt, depth within the ejecta blanket, and whether the sample was altered. Impact melts collected on or near the surface and later analyzed by Hörz and others (2002) were interpreted to have been pervasively hydrated and oxidized long after the impact. However, more than half of our sample suite of impact-melt particles collected from drill cuttings do not appear to have experienced considerable alteration, based on texture and composition. Because altered impact melts occur in proximity to non-altered melts, there is the question of when alteration took place. If alteration is occurring in situ, does this illustrate how percolating fluids disperse when migrating through the subsurface? Compositional heterogeneities in impact melts reflect the chaotic nature of excavation and

ejecta emplacement processes, resulting in unique thermal and geochemical histories for each individual impact-melt fragment (French, 1998).

Crystalline Groundmass

Most impact melts have a crystalline groundmass that is composed of Ca-rich pyroxene and Fe-rich olivine, minerals found only in the impact melts. The Coconino Sandstone, the Kaibab Formation, and the Moenkopi Formation are all sedimentary in origin, and as such, olivine and pyroxene do not naturally occur in the vicinity of Meteor Crater (Shoemaker and Kieffer, 1974; Roddy, 1978; Morris and others, 2000). Therefore, the origin of these minerals is from the melting and mixing of the meteorite and target rocks (French, 1998; Hörz and others, 2002), creating a mafic melt ripe for the crystallization of olivine and pyroxene. The crystal habits of these minerals (skeletal or acicular) suggests these phases nucleated, grew, and quenched in a rapid manner (Lofgren, 1980). Many of the granular pyroxene crystals have inclusions of skeletal olivine, indicating that olivine nucleated first, followed by pyroxene.

Carbonate and Barium Sulfate Inclusions

The abundance of carbonate inclusions (CIs) and barium sulfate was an unanticipated find. Nearly 70 percent of analyzed samples had carbonate inclusions observed in more than one grain within each mount. We do not have an estimate on the percentage of barium sulfate inclusions within CIs, but it was a common occurrence. The origin of CIs in impact melts at Meteor Crater is still questioned, whether they are melted dolomite (from the Kaibab Formation) that did not volatilize during the time of the impact (Osinski and others, 2008, 2015), or precipitated through low-temperature secondary processes, long after the impact (Hörz and others, 2002, 2015).

Carbonates analyzed by Hörz and others (2002, 2015) render slight differences in composition compared to most of the CIs we analyzed. One primary difference was the concentrations of minor elements, such as Mg and Si, in addition to traces of the meteorite. Hörz and others (2002, 2015) determined that their population of carbonates was calcite, with anomalously high SiO_2 concentrations (2–7 weight percent SiO_2), typically <2 weight percent MgO, and completely void (or below the detection limit) of FeO and NiO. This, in addition to being attributed to vesicle infill, led Hörz and others (2002, 2015) to conclude these carbonates were the product of secondary processes (such as through the weathering of soils and rocks by rainwater, low-temperature calcium carbonates can precipitate). The presence of SiO_2 and Al_2O_3 impurities can be explained by the presence of clay minerals that are typically intermixed with high-desert soils (Sancho and others, 1992).

CIs found in impact melts recovered from deep within the ejecta blanket ranged from ~20 weight percent MgO to negligible amounts (fig. 11), with the average being ~4 weight percent MgO. Some melt particles had a carbonate coating or rind, which yielded slightly higher amounts of SiO_2 and Al_2O_3 when compared to CIs (fig. 12) and averaged 3 weight percent MgO. Minor amounts of FeO and NiO were detected in both the rinds and inclusions. Ni concentrations for most inclusions and rinds were below the detection limit of the electron microprobe (which is ~0.03 weight percent), though of the total number of carbonate inclusions we measured, ~28 percent had NiO concentrations of 0.04–1.3 weight percent. FeO concentration ranged from negligible amounts to around 1.5 weight percent FeO, with one outlier of 3.4 weight percent.

We infer that CIs situated within or along the margins of partially melted lithics (for example, Kaibab Formation clasts, with dolomite and quartz present) likely have an impact-related origin based on their spatial relationship to such lithics (fig. 10*B,C*). On the other hand, CIs that are not associated with partially melted lithics or individual mineral grains, but instead have barium sulfate inclusions, may differ in their origin. The euhedral, tabular habit of barium sulfate crystals within CIs does not support a pre-impact origin in which these crystals were entrained in the impact melt; rather, they likely precipitated in situ along vesicle walls prior to or concurrently with carbonate infill (Brock-Hon and others, 2012). The occurrence of barium sulfate in arid environments has been observed as infill within pore-void spaces, as well as precipitating as tabular crystals lining circular pore spaces that are partially filled with calcium carbonate, typically around 1–2 m depth within the soil horizon (Mees and Tursina, 2010; Brock-Hon and others, 2012).

Mittlefehldt and others (2005) carried out trace element analyses of target rocks and some impact melts and found that barium concentrations were typically less than 400 µg/g in target rocks, whereas impact melts ranged from <100 to 13,400 µg/g. Impact-melt particles enriched in barium were noted by Mittlefehldt and others (2005) to have secondary minerals infilling vesicles and coating the exterior of the fragments, providing a likely explanation for the influx of barium. A possible source for increased concentrations of both barium and sulfur could be dust. Arid environments commonly have dust coating the ground, which can undergo dissolution, leading to the mobilization of barium and sulfur ions that can then re-precipitate at depth (Brock-Hon and others, 2012).

Isotopic analyses for C and O in CIs (for example, Hörz and others, 2015) and S (for example, Craddock and others, 2008) in barium sulfate inclusions can be used to derive the origin of these phases, whether they are related to the impact or from post-impact secondary processes.

Quartz

Target rocks at Meteor Crater are rich in quartz (that is, Coconino Sandstone, thin layers of calcareous sandstone within the Kaibab Formation, and siltstone and sandstone

comprising the Moenkopi Formation), causing silica to be ubiquitous in impact-melt particles. Quartz grains within each of the target rock groups have experienced a range of pressures and temperatures generated during the contact, compression, and excavation stages of crater formation. These conditions led to different stages of shock metamorphism within the silica structure. Kieffer (1971) details the different classes of shocked silica-rich rocks, ranging from weakly shocked and fractured quartz grains to the conversion of coesite or stishovite (high pressure and temperature silica phases), and finally shock-melted glass (lechatelierite). Much of the texture variations of silica are correlated to these classes (Kieffer, 1971).

Metallic Inclusions

Small, rounded to irregular in shape metallic inclusions (MIs) were the last features described in this report. MIs we have analyzed here are most like the impactite metallic particles described by Kelly and others (1974). We observed two and sometimes three different phases within the bounds of each metallic inclusion and labeled them as dark, intermediate, and bright (which is how they appear in the SEM). MIs consist predominately of the bright phase, an Fe-Ni alloy that varies in concentration between these two metals (fig. 15) and displays a skeletal texture (fig. 14) (Vdovykin, 1973). The intermediate phase, an Fe-Ni sulfide, is interstitial among the Fe-Ni alloy. The dark phase is the least common and has been observed both in the interstitial spaces and as inclusions along the interior boundaries of the metal alloy (fig. 14).

Data Availability

Using a SEM and electron microprobe, we characterized 42 impact-melt particles that were acquired from the USGS Astrogeology Science Center Meteor Crater sample collection. We carried out detailed imaging for all 42 particles, EDS compositional analyses for 30 of these samples, and WDS compositional analyses for 21 samples. Geochemical data includes the compositions of glass, carbonate inclusions, metallic inclusions, barium sulfate, groundmass (both olivine and pyroxene), and a miscellaneous category for uncommon phases (for example, zircon, potassium feldspar). The full set of WDS and EDS compositional data and annotated BSE images are available in ScienceBase as a data release (Gullikson and others, 2024) and can be found at https://doi.org/10.5066/P9OGAJ8P.

The complete Meteor Crater sample collection database can be accessed at https://www.usgs.gov/data/meteor-crater-northern-arizona-drill-hole-sample-collection-1970-1973-and-curation-2010-2013 (Gaither and others, 2023). All samples within the collection, including impact-melt particles highlighted in this report, can be acquired for scientific research. More information on how to request samples can be found at the USGS Astrogeology Science Center Meteor Crater sample collection website (https://www.usgs.gov/centers/astrogeology-science-center/science/meteor-crater-sample-collection).

References Cited

Artemieva, N., and Pierazzo, E., 2009, The Canyon Diablo impact event—Projectile motion through the atmosphere: Meteoritics and Planetary Science, v. 44, p. 25–42. https://doi.org/10.1111/j.1945-5100.2009.tb00715.x

Brock-Hon, A.L., Robins, C.R., and Buck, B.J., 2012, Micromorphological investigation of pedogenic barite in Mormon Mesa petrocalcic horizons, Nevada USA—Implication for genesis: Geoderma, v. 179–180, p. 1–8. https://doi.org/10.1016/j.geoderma.2012.02.012

Craddock, P.R., Rouxel, O.J., Ball, L.A., and Bach, W., 2008, Sulfur isotope measurement of sulfate and sulfide by high-resolution MC-ICP-MS: Chemical Geology, v. 253, p. 102–113. https://doi.org/10.1016/j.chemgeo.2008.04.017

French, B.M., 1998, Traces of Catastrophe—A handbook of shock-metamorphic effects in terrestrial meteorite impact structures: Houston, Lunar and Planetary Institute Contribution, no. 954, 120 p.

Gaither, T.A., Gullikson, A.L., Hagerty, J.J., Roddy, D.J., and Boyce, J.M., 2023, Meteor Crater, Northern Arizona—Drill hole sample collection, 1970–1973, and curation, 2010–2013: U.S. Geological Survey data release, accessed December 19, 2023, at https://doi.org/10.5066/P9SWO5OO.

Grant, J.A., and Schultz, P.H., 1990, Amounts and styles of ejecta erosion at Meteor Crater, Arizona [abs.], *in* Abstracts of the Lunar and Planetary Science Conference, 21st: Lunar and Planetary Science Institute, abstract no. 1222, p. 433–434.

Grant, J.A., and Schultz, P.H., 1993, Erosion of ejecta at Meteor Crater, Arizona, Journal of Geophysical Research, v. 98, no. E8, p. 15033–15047. https://doi.org/10.1029/93JE01580

Grieve, R.A.F., Dence, M.R., and Robertson, P.B., 1977, Cratering processes—As interpreted from the occurrence of impact melts, *in* Roddy, D.J., Pepin, R.O., and Merrill, R.B., eds., Impact and explosion cratering: New York, Pergamon Press, p. 791–814.

Gullikson, A.L., Gaither, T.A., Villarreal, K.A., and Hagerty, J.J., 2016, Lithostratigraphic analysis of the Meteor Crater ejecta blanket [abs.], *in* Proceedings of the Lunar and Planetary Science Conference, 47th: Lunar and Planetary Science Institute, abstract no. 1541.

Gullikson, A.L., Gaither, T.A., and Hagerty, J.J., 2024, Geochemistry and high-resolution backscattered electron imaging of Meteor Crater impact melts: U.S. Geological Survey data release, accessed March 26, 2024, at https://doi.org/10.5066/P9OGAJ8P.

Hermalyn, B., Schultz, P.H., Anderson, J.L.B., and Heineck, J.T., 2008, Time-resolved assessment of ejecta-mass distribution using 3D-PIV [abs.], *in* Proceedings of the Lunar and Planetary Science Conference, 39th: Lunar and Planetary Science Institute, abstract no. 2292.

Hörz, F., Mittlefehldt, D.W., See, T.H., and Galindo, C., 2002, Petrographic studies of the impact melts from Meteor Crater, Arizona, USA: Meteoritics and Planetary Science, v. 37, p. 501–531. https://doi.org/10.1111/j.1945-5100.2002.tb00836.x

Hörz, F., Archer, P.D.Jr., Niles, P.B., Zolensky, M.E., and Evan, M., 2015, Devolatilization or melting of carbonates at Meteor Crater, AZ? Meteoritics and Planetary Sciences, v. 50, no. 6, p. 1050–1070. https://doi.org/10.1111/maps.12453

Kelly, W.R., Holdsworth, E., and Moore, C.B., 1974, The chemical composition of metallic spheroids and metallic particles within impactite from Barringer Meteorite Crater, Arizona: Geochimica et Cosmochimica Acta, v. 38, p. 533–543. https://doi.org/10.1016/0016-7037(74)90039-8

Kieffer, S.W., 1971, Shock metamorphism of the Coconino Sandstone at Meteor Crater, Arizona: Journal of Geophysical Research, v. 76, no. 23, p. 5449–5473, accessed March 26, 2024 at https://doi.org/10.1029/JB076i023p05449.

Kingma, K.J., and Hemley, R.J., 1994, Raman spectroscopic study of microcrystalline silica: American Mineralogist, v. 79, no. 3–4, p. 269–273.

Kring, D.A., 2007, Guidebook to the geology of Barringer Meteorite Crater, Arizona (a.k.a Meteor Crater)—70th Annual Meeting of the Meteoritical Society, Tucson, Ariz., August 13–17, 2007: Houston, Tex., Lunar and Planetary Institute, LPI Contribution No. 1355, p. 150

Lofgren, G., 1980, Experimental studies on the dynamic crystallization of silicate melts, *in* Hargraves, R.B., ed., Physics of magmatic processes: Princeton, New Jersey, Princeton University Press, p. 487–552. https://doi.org/10.1515/9781400854493.487

Mead, C.W., Littler, J., and Chao, E.C.T., 1965, Metallic spheroids from Meteor Crater, Arizona: American Mineralogist, v. 50, p. 667–681.

Mees, F. and Tursina, T.V., 2010, Salt minerals in saline soils and salt crusts, *in* Stoops, G., Marcelino, V., and Mees, F., eds., Interpretation of micromorphological features of soils and regoliths: The Netherlands, Elsevier, p. 441–469. https://doi.org/10.1016/B978-0-444-53156-8.00020-9

Melosh, H.J., 1980, Cratering mechanics—Observational, experimental, and theoretical: Annual Review of Earth and Planetary Sciences, v. 8, p. 65–93. https://doi.org/10.1146/annurev.ea.08.050180.000433

Melosh, H.J., 1989, Impact cratering—A geologic process: New York, Oxford University Press, 78 p.

Melosh, H.J. and Collins, G.S., 2005, Meteor Crater formed by a low-velocity impact: Nature, v. 434, p. 157. https://doi.org/10.1038/434157a

Mittlefehldt, D.W., Hörz, F., SeeT.H., Scott, E.R.D., and Mertzman, S.A., 2005, Geochemistry of target rocks, impact melt particles, and metallic spherules from Meteor Crater, Arizona—Empirical evidence on the impact process: Geological Society of America Special Paper 384, p. 367–390.

Morris, R.V., Golden, D.C., Bell, J.F., III, Shelfer, T.D., Scheinost, A.C., Hinman, N.W., Furniss, G., Mertzman, S.A., Bishop, J.L., Ming, D.W., Allen, C.C., and Britt, D.T., 2000, Mineralogy, composition, and alteration of Mars Pathfinder rocks and soils—Evidence from multispectral, elemental, and magnetic data on terrestrial analogue, SNC meteorite, and Pathfinder samples: Journal of Geophysical Research, v. 105, no. E1, p. 1757–1817, accessed March 26, 2024, at https://doi.org/10.1029/1999JE001059.

Newsom, H.E., Wright, S.P., Misra, S., and Hagerty, J.J., 2012, Comparison of simple impact craters—A case study of Meteor and Lonar Craters, chap. 18 *of* Osinski, G.R., and Pierazzo, E., eds., Impact cratering—Processes and products: Hoboken, N.J., Wiley-Blackwell, p. 271–289.

Nininger, H.H., 1956, Arizona's Meteorite Crater—Past, present, and future: Sedona, Arizona, American Meteorite Museum, 232 p.

Nishiizumi, K., Kohl, C.P., Shoemaker, E.M., Arnold, J.R., Klein, J., Fink, D., and Middleton, R., 1991, In situ ^{10}Be-^{26}Al exposure ages at Meteor Crater, Arizona: Geochimica et Cosmochimica Acta, v. 55, p. 2699–2703. https://doi.org/10.1016/0016-7037(91)90388-L

Osinski, G.R., Grieve, R.A.F., and Spray, J.G., 2008, Impact melting in sedimentary target rocks—An assessment: Geological Society of America Special Paper 437, p. 1–17.

Osinski, G.R., Bunch, T.E., Flemming, R.L., Buitenhuis, E., and Wittke, J.H., 2015, Impact melt- and projectile-bearing ejecta at Barringer Crater, Arizona: Earth and Planetary Science Letters, v. 432, p. 283–292. https://doi.org/10.1016/j.epsl.2015.10.021

Phillips, F.M., Zreda, M.G., Smith, S.S., Elmore, D., Kubik, P.W., Dorn, R.I., and Roddy, D.J., 1991, Age and geomorphic history of Meteor Crater, Arizona, from cosmogenic 36Cl and 14C in rock varnish: Geochimica et Cosmochimica Acta, v. 55, p. 2695–2698. https://doi.org/10.1016/0016-7037(91)90387-K

Ramsey, M.S., 1995, Ejecta distribution at Meteor Crater, Arizona, derived from thermal infrared multispectral scanner data: The Compass, v. 71, no. 2, p. 69–80.

Ramsey, M.S., 2002, Ejecta distribution patterns at Meteor Crater, Arizona—On the applicability of lithologic end-member deconvolution for spaceborne thermal infrared data of Earth and Mars: Journal of Geophysical Research, v. 107, no. E8, p. 3–1 to 3–14, accessed on November 16, 2023, at https://doi.org/10.1029/2001JE001827.

Roddy, D.J., 1978, Pre-impact geologic conditions, physical properties, energy calculations, meteorite and initial crater dimensions and orientations of joints, faults and walls at Meteor Crater, Arizona, *in* Merrill, R.B., ed., Proceedings of the. Lunar Planetary Science Conf., 9th: New York, Pergamon Press, p. 3891–3930.

Roddy, D.J., Boyce, J.M., Colton, G.W., and Dial, A.L., Jr., 1975, Meteor crater, Arizona, rim drilling with thickness, structural uplift, diameter, depth, volume, and mass-balance calculations, *in* Merrill, R.B., Hubbard, N.J., Mendell, W.W., and Williams, R.J., eds., Proceedings of the Lunar Science Conference, 6th: New York, Pergamon Press, p. 2621–2644.

Sancho, C., Melendez, A., Signes, M., and Bastida, J., 1992, Chemical and mineralogical characteristics of Pleistocene caliche deposits from the central Ebro Basin, NE Spain: Clay Minerals, v. 27, p. 293–308. https://doi.org/10.1180/claymin.1992.027.3.03

See, T.H., Hörz, F.Mittlefehldt, D.W., Varley, L., Mertzman, S., and Roddy, D., 2002, Major element analyses of the target rocks at Meteor Crater, Arizona: National Aeronautics and Space Administration, NASA/TM-2002–210787, 23 p.

Shoemaker, E.M., 1960, Impact mechanics at Meteor Crater Arizona: Princeton, New Jersey, Princeton University, Ph.D. dissertation, 55 p.

Shoemaker, E.M., and Kieffer, S.W., 1974, Guidebook to the geology of Meteor Crater, Arizona: Tempe, Ariz., Arizona State University Center for Meteorite Studies, publication 17, 66 p.

Vdovykin, G.P., 1973, The Canyon Diablo meteorite: Space Science Reviews, v. 14, p. 758–831. https://doi.org/10.1007/BF00224776.

Moffett Field Publishing Service Center
Manuscript approved September 13, 2024
Edited by Eneas Andrade
Layout and design by Cory Hurd
Publication support by Timothy Herold

ISSN 2331-1258 (online)
https://doi.org/10.3133/ofr20241062